Yifan Fan., Julian Hunt., Qun Wang., Yuguo Li. (2020)
Inversion breakup over different shapes of urban areas. *Building and Environment.* doi: 10.1016/j.buildenv.2020.107548

Inversion breakup over different shapes of urban areas

Yifan Fan

Julian Hunt

Qun Wang

Yuguo Li

College of Civil Engineering and Architecture, Zhejiang University, Hangzhou, China

Department of Mechanical Engineering, The University of Hong Kong, Hong Kong SAR, China

Department of Earth Sciences, University College London, London, UK

Malaysian Commonwealth Studies Centre, Cambridge, UK

International Research Center for Green Building and Low-Carbon City, International Campus, Zhejiang University, China

Corresponding author: Yuguo Li, Department of Mechanical Engineering, The University of Hong Kong, Hong Kong SAR, China

Email: liyg@hku.hk (Y. Li).

Subumitted to *Building and Environmen* 24 September 2020

Accepted 19 December 2020

Author biographies

Yifan Fan, PhD, is Professor in College of Civil Engineering and Architecture, Zhejiang University. His research interests are urban heat island, urban climate, urban ventilation, urban and built environment.

Julian Hunt, PhD, FRS, is Emeritus Professor of Climate Modelling in the Department of Earth Sciences and Honorary Professor of Mathematics at University College London, London, United Kingdom. His research interests are in meteorology, fluid mechanics, and turbulence. His current research topics include climate and weather prediction, wind flow in urban environments, pollutant dispersion, and ocean wave dynamics.

Qun Wang, PhD, is an Assistant Professor in the Department of Environmental Science and Engineering, Macau University of Science and Technology. His research interests include high-resolution urban thermal environments, climate-change impacts on urban systems and air quality.

Yuguo Li, PhD, is Chair Professor of Building Environment, Honorary Professor of School of Public Health, Associate Dean (Research) of Engineering in the University of Hong Kong. His research interests are in building environment engineering. His current research topics include city climate/environment, environment studies of infection and indoor environment.

Inversion breakup over different shapes of urban areas

Abstract

Severe haze episodes and extreme heat events are both related to the strong inversion in the atmospheric boundary layer. Inversion breakup is the main mechanism to alleviate the accumulation of heat or pollutants, especially in urban areas. However, the physical process and turbulent flow structures of inversion breakup remain unclear. In this study, the characteristics of mean flow structures and turbulence statistics of inversion breakup at the two-dome stage were investigated by conducting reduced-scale water tank experiments. A two-layer density profile (i.e. a lower-level stable layer and an upper-level neutral layer) was created to simulate the surface-based inversion covered by a neutral residual layer. Various shapes of urban areas were tested. The results showed that the lower-level dome in the stable layer (Dome 1) and the upper-level dome in the neutral layer (Dome 2) are both substantially affected by the urban shape. In Dome 1, the convergent inflow is mainly along the angular bisector across the urban corners, whereas the divergent outflow is perpendicular to the edges. In Dome 2, the divergent outflow is on the same vertical plane with the convergent inflow (i.e. along the angular bisector). Furthermore, the turbulence production and momentum transfer are mainly induced by the thermal plume structures near the urban centre, indicating the strong influences of buoyancy. In divergent outflow regions, both shear and buoyancy play important roles.

(224 words)

Keywords: Inversion breakup; Urban heat island circulation; Dome; Urban shape effect

Introduction

Due to intensive human activities, the underlying surface in urban areas has been considerably modified, which has resulted in a distinct urban climate. Consequently, various urban-specific environmental islands have arisen, such as the urban heat island or urban heat dome (UHI, Bornstein 1968; Oke 1973; Fan et al. 2017b), urban cool island (UCI, Lindén 2011; Yang et al. 2016; Rasul et al. 2017), urban pollution island or urban pollution dome (UPI, Megaw 1977; Li et al. 2018; Huang et al. 2019), urban moist or moisture island (UMI, Deosthali 2000; Wang et al. 2020), urban dry island (UDI, Wang and Gong 2010; Lokoshchenko 2017; Hao et al. 2018) and urban CO_2 island or urban CO_2 dome (UCO_2I, Idso et al. 2001, 2013; Jacobson 2010). These 'islands' trap heat, moisture and airborne pollutants over a city below a certain height, and modulate the urban thermal and wind environment, as well as pollutant dispersion and the pollutant exposure of residents (Hang et al. 2017).

With the increasing frequency of extreme heatwaves and haze episodes, the UHI, UPI and UCO_2I effects are attracting more attention. Their intensities can be amplified by the stable background stratification or inversion, as the stable layer suppresses turbulence and vertical dispersion (Founda and Santamouris 2017; Fan et al. 2020; Chen et al. 2020).

There are two types of inversion: surface-based inversion (SBI) and elevated inversion (EI). SBI is formed due to the surface cooling of longwave radiation (Czarnecka and Nidzgorska-Lencewicz 2017), and thus usually shows a clear diurnal cycle (Palarz et al. 2019), whereas EI is mainly induced by the subsidence of large-scale atmospheric circulation in a high-pressure system (Largeron and Staquet 2016) and can last several days. EI can also be formed by other factors, such as cold/warm fronts (Fan et al. 2019a) or the combined effect of surface radiative cooling and urban mixing layer (Godowitch et al. 1985). SBI is usually stronger (larger buoyancy frequency) and thinner (smaller inversion layer depth) than EI (Palarz et al. 2019; Khalesi and Daneshvar 2020). SBI and EI can be present simultaneously. According to the measurements conducted by Weston et al. (2020), SBI occurs near the surface (0–100 m), EI occurs at heights of 500–1500 m, and a neutral layer (residual layer) lies in between. Normally, the depth of SBI ranges from 100 to 600 m and that of the neutral layer aloft is in the range of 400-1000 m. Therefore, the ratio of SBI depth to the neutral layer aloft depth is approximately 1/10–3/2. Khalesi and Daneshvar (2020) recorded five-year data (2014.1.1–2018.12.31) on atmospheric stability in Tehran and found that inversion was present on 74% of the days (SBI: 77%, EI: 23%). The strength of the inversion can be quantified using buoyancy frequency N (s^{-1}). A typical value of N is 0.015 s^{-1} (Hunt et al. 1988). Larger values (0.028-0.045 s^{-1}) have also often been recorded (Li et al. 2019; Khalesi and Daneshvar 2020) and an extreme value of 0.1 s^{-1} is rarely observed (Clements et al. 2003).

The breakup of inversion alters the characteristics of heat transfer and pollutant

concentration. Inversion breakup enhances turbulent mixing, and thus, heat transfer between the atmosphere and underlying surfaces (Fan et al. 2019a, c, 2020; Krüger and Emmanuel 2013). Regarding pollutant concentration, inversion breakup can either increase or decrease pedestrian-level pollutant concentrations, depending on the position of the pollutant source (Figure 1). If the pollutants are concentrated in the near-surface region or the pollution sources are ground-based, such as traffic emissions, the inversion breakup will enhance mixing and pollutant dispersion, and thus reduce pedestrian-level pollution (Figure 1a). According to Li et al. (2019), the aerosol concentration reduces by 58% in winter and 18% in summer, on average, in the absence of inversion. Janhäll et al. (2006) also suggested that the pollutant concentration can be increased by 4-10 times with inversion during the morning rush hour, when the pollutants are mainly created by traffic. A $PM_{2.5}$ concentration of 10000 μg m^{-3} was recorded at a fireworks event under a stable stratification condition (Hoyos et al. 2019). If there are elevated pollutant sources above the lower stable layer, such as an ultra-high chimney, an airplane and remaining pollutants from previous days or regional transport (Allen and Holmes 2015), inversion breakup can result in fumigation, which increase pedestrian-level pollution (Figure 1b). Various studies have measured the fumigation of atmospheric pollutants after inversion breakup, e.g., Hg (Snyder et al. 2008), O_3 (Evans 1979) and $ClNO_2$ (Tham et al. 2016; Osthoff et al. 2018) (Peters 1975).

<Fig. 1>

Both strong synoptic wind and the underlying heating from the surface can break inversions. Here, we focus on the physical process of inversion breakup due to heating, which is described as follows. During a calm clear night in a rural area, SBI is usually formed, whereas a shallow mixing layer topped by an elevated inversion (in the form of a dome shown in Figure 1ai) is sustained under the urban heat island effect (Godowitch et al. 1985). In the morning after sunrise, the inversion layer can be eroded by the mixing layer over the urban area if excess energy is continuously supplied to the mixing layer (Leukauf et al. 2016). During the erosion process, the mixing layer grows gradually and lifts up the above inversion layer. Meanwhile, gradually, the base of the inversion layer (i.e. the top of the mixing layer) becomes higher and the inversion layer becomes thinner. The mixing layer grows rapidly (Figure 1aii) after the total erosion of the inversion layer (Godowitch et al. 1985).

Although a considerable number of studies suggest that inversion breakup is important for heat and mass transfer in the atmospheric boundary layer (Whiteman 1982; Leukauf et al. 2015; Rendón et al. 2015; Wang et al. 2018), detailed flow structures have been rarely studied. By conducting water tank experiments, Fan et al. (2019a) first found three stages during the inversion breakup process over a circular urban area: the two-dome stage, wing-shrinking stage and perforative-plume stage. Moreover, the shape of the urban area has been found to affect the mean and turbulent flow structures of the urban dome flow (Fan et al. 2018b, 2019c). Therefore, whether the shape of the urban area affects the inversion breakup process needs to be clarified. This paper focuses on

investigating the influences of urban area shape on the mean and turbulent flow structures at the two-dome stage.

2. Methods

In this study, water tank experiments were conducted. Reduced-scale water tank experiments have proved to be an effective method to investigate the flow structures of a convective boundary layer (CBL, Willis and Deardorff 1974), urban heat island-induced circulation (UHIC, Lu et al. 1997b; Fan et al. 2016b), inversion breakup (Fan et al. 2019a; Princevac and Fernando 2008; Fernando 1987), sea breeze circulation (Cenedese and Monti 2003), slope flow (Reuten 2006), flow–mountain interaction (Hunt et al. 1988) and pollutant dispersion (Zhang and Sang 1999, 2004; Xuan and Zhang 1999). The similarity between the reduced-scale model and prototype has been well established (Fan et al. 2016b, 2019a; Lu et al. 1997b; Cenedese and Monti 2003).

The water tank had dimensions of 1.2(length) × 1.2(width) × 1.1(height) m, as illustrated in Figure 2a. According to Fan et al. (2019c) and Lu et al. (1997b), this size of water tank is large enough to eliminate the influence of lateral walls on the urban heat dome flow.

<Fig. 2>

Six cases with different heater shapes were designed, with reference to Fan et al. (2019c). The geometry parameters and coordinate system in terms of the layout of the urban areas are indicated in Figure 3.

<Fig. 3>

Cases 2 and 3 were set to have the same geometry but different orientations towards Camera 1, so that the velocity fields along both the long and short sides could be measured. Cases 4 and 5 were similarly arranged for the same reason.

The velocity field was measured using the particle image velocimetry (PIV) system, which comprises a high-speed camera and a laser. As shown in Figure 2a, there were two cameras and lasers, which formed two sets of acquisition systems to rapidly obtain velocity fields on the horizontal and vertical planes. Camera 1 (Speed Sense M140 model, 2560 × 1600 pixels, Dantec Dynamics A/S, Skovlunde, Denmark) with a prime lens (35 mm focal length, f/1.8 maximum aperture, AF-S DX Nikkor, Nikon Imaging Japan Inc., Japan) and Laser 1 (3 W DPSS 532 nm laser projector, Ourslux Lighting Technology Co, Ltd, Shenzhen, China) were used to measure the velocity field on the vertical plane across the middle of the heated urban centre. Camera 2 (Speed Sense M140 model, 2560 × 1600 pixels, Dantec Dynamics A/S, Skovlunde, Denmark) with a prime lens (20 mm focal length, f/1.8 maximum aperture, AF-S Nikkor, Nikon Imaging Japan Inc., Japan) and Laser 2 (RayPower 10W 532-nm continuous green laser, Dantec

Dynamics A/S, Skovlunde, Denmark) were used to obtain the velocity field on the horizontal plane. Camera 2 and Laser 2 were placed on a traverse device so that they could move simultaneously to measure the velocity fields at different levels without re-focusing. The seeding particles used were 20-μm Polyamid Seeding Particles (PSP-20 μm, Dantec Dynamics A/S, Skovlunde, Denmark). Both cameras operated continuously at 30 Hz for 30 s (total 900 images in a single run), under limited camera memory and convective speed magnitude (Fan et al. 2019a,c). After one run, the captured 900 images were transferred from the camera memory to the hard disk of the computer, and then the camera memory was cleared ready for the next run. After the experiments, the captured particle images were analysed with the commercial software Dynamic Studio (Dantec Dynamics A/S, Skovlunde, Denmark). The adaptive PIV algorithm was selected to calculate the maximum correlation between two consecutive images and obtain the velocity field. A detailed description of the algorithm, parameters and uncertainty analysis can be found in Fan et al. (2019a).

The cross-section of the water tank is shown in Figure 2b, which presents a detailed structure of the heated area. The heat source was a 2-cm-deep copper thermal resistance heater (yellow colour in Figure 2b), controlled by a transformer to provide the desired heat flux. There was a 1-cm flat copper plate (red colour in Figure 2b) above the heater to make the temperature over the surface as uniform as possible by taking advantage of the high thermal conductivity of copper. On the upper surface of the copper plate, a layer of black matte paint was sprayed to reduce the light reflectance, avoid overexposure on images in the near-surface region and thus improve the quality of the particle images.

The heater and copper plate were surrounded by a silica gel pad below and a polyvinyl chloride (PVC) plate in the lateral direction to reduce the heat leakage. Thermocouples were deployed in the location marked in Figure 2b to monitor the temperature of the urban area and that of the ambient environment. The temperature data from the thermocouples were recorded using an Agilent 34972A data logger (Keysight, Santa Rosa, CA) at an acquisition frequency of 1 Hz. The value of the supplied heat flux P_s (W m^{-2}) in six cases was obtained by measuring the voltage and current of the heater, as shown in Table 1. According to Fan et al. (2019c), the leakage heat flux P_l (W m^{-2}) can be estimated as

<Table 1>

$$P_l = \lambda_s \left(T_s - T_a\right) / z_s \quad (1)$$

where λ_s (0.17 W m^{-1} K^{-1}) is the thermal conductivity of the silica gel plate. T_s (°C) is the average temperature measured by thermocouples TC 1 and TC 2, shown in Figure 2b and T_a (°C) is the ambient temperature obtained by thermocouple TC 3. z_s (0.01 m) is the thickness of the silica gel plate. The heat flux released into the fluid

through the urban area can be calculated as $H_0 = P_s - P_l$.

The convective velocity scale u_d and Froude number Fr are important parameters that indicate whether the reduced-scale model is similar and representative of real-scale atmospheric flows (Lu et al. 1997a). These three parameters are introduced in detail as follows. u_d (m s^{-1}) and Fr are defined as Eqs (2) and (3), respectively (Lu et al. 1997a; Cenedese and Monti 2003; Colomer et al. 1999).

$$u_d = \left[g\beta d H_0 / \left(\rho_0 c_P \right) \right]^{1/3} \quad (2)$$

where ρ_0 (kg m^{-3}), c_P (J kg^{-1} K^{-1}) and β (K^{-1}) indicate the reference density, specific heat capacity and thermal expansion rate of the fluid, respectively. $d = 4A/L$ is the hydraulic diameter. A (m^2) and L (m) are the area and perimeter of the heat source, respectively, and g (m s^{-2}) is the acceleration of gravity.

$$\mathrm{Fr} = u_d / \left(Nd \right) \quad (3)$$

where ρ (kg m^{-3}) is the fluid density and z (m) is the vertical coordinate. N (s^{-1}) is the buoyancy frequency of stable stratification and is defined as $N = \sqrt{-\left(g/\rho_0 \right) \partial \rho / \partial z}$ (Stull 1988). Two-layer stratification is created, with the lower layer being stably stratified (density decreases with height linearly) and the upper layer being neutral (density is constant), which is designed to simulate the SBI near the ground and neutral residual layer aloft. The depths of the stable layer and neutral layer aloft are 4 and 12 cm, respectively. The detailed methods for creating two-layer stratification and the advantages of using salt water to simulate the stratification can be found in Fan et al. (2019a). The density gradient of the lower stable layer is used to calculate the buoyancy frequency. The vertical density profiles of the six cases are shown in Figure 4. Density data were measured with a conductivity and temperature sensor (MSCTI, PME, Inc., Vista, CA, USA). For the procedures of using MSCTI for the calibration and measurements, please refer to Fan et al. (2018a).

<Fig. 4>

The density gradient is fitted with the density data in the stable layer (below the blue dash line in Figure 4). The fitted gradients ($\partial \rho / \partial z$, and accordingly, R^2) for the six cases are 71.78 kg m^{-4} (0.9958), 89.72 kg m^{-4} (0.9798), 82.28 kg m^{-4} (0.9951), 51.96 kg m^{-4} (0.9861), 57.51 kg m^{-4} (0.9929) and 53.34 kg m^{-4} (0.9937), respectively. The values of u_d and Fr are summarised in Table 1.

According to Fan et al. (2020), the urban heat dome flow can be appropriately

simulated if Fr < 0.08. In our study, Fr ranges 0.047–0.078, which satisfies the mentioned criterion. As analysed in Fan et al. (2019c), the Fr in our experiments (0.047-0.078) can represent a real city scale of 7-15 km (hydraulic diameter of the city) under typical background conditions of $N = 0.005$ s^{-1} and H_0=100 W m^{-2} (Hunt et al. 1988; Reuten 2006; Hidalgo et al. 2008b; Christen et al. 2003; Oke et al. 1999; Fan et al. 2019c). In this study, the ratio of the stable layer depth to the above neutral layer depth was fixed at 1/3 (4/12 cm), which is within the range of a real atmospheric condition (approximately 1/10–3/2) (Weston et al. 2020).

3. Results

3.1 Mean velocity field

3.1.1 Vertical plane

As found in Fan et al. (2018b, 2019c), the shape of the urban area substantially affects the structure of urban dome flows. Generally, an urban dome flow has a lower-level convergent inflow, an upper-level divergent outflow and an upward-rising flow at the urban centre (Lu et al. 1997a; Fan et al. 2016b, 2017a, 2019; see Figure 1a(i) and 1b(i)). For the urban dome flow over a polygon urban area, the lower-level inflows are mainly along the direction of the angular bisector, whereas the upper-level outflows are perpendicular to the edges (Fan et al. 2019c). As for the processes of inversion breakup, there are three stages (Fan et al. 2019a): a two-dome stage (Stage 1), wing-shrinking stage (Stage 2) and perforative-plume stage (Stage 3). Stage 2 is a transitional stage, whereas the lower stable layer is totally destroyed in Stage 3. The characteristics of the flow in Stage 3 are the same as those of the thermal plume structure in a neutral background environment. In Stage 1, the urban dome flow is maintained in the lower stable layer, i.e. Dome 1. Meanwhile, another dome flow in the neutral layer aloft is initiated, i.e. Dome 2. Therefore, it is more appropriate to study the shape effect on the inversion breakup process during Stage 1, and hence, the differences in the flow structures at the two-dome stage are mainly focused and compared. The mean velocity fields (30 s average from 900 captured images in one run) at the two-dome stage across the urban centre of the six cases are shown in Figure 5. The arrows and colour represent the average velocity vectors and mean speed S ($\sqrt{u^2 + w^2}$), respectively, where u and w are the horizontal (x-direction) and vertical (z-direction) velocity components, respectively.

<Fig. 5>

Case 1 (Figure 5a) shows the flow over a circular urban area. Domes 1 and 2 are present in the lower stable layer and upper neutral layer, respectively, similar to the case in Fan et al. (2019a). Dome 1 is formed due to the lower-level stable stratification, whereas the vertical dimension of Dome 2 is limited by the water–air interface. Both inflows and outflows appear in Domes 1 and 2 on the measured

vertical plane across the urban centre (Figure 5a). There is a clear shear region between the outflow of Dome 1 and inflow of Dome 2, located on the interface between the lower stable layer and upper neutral layer, marked by a dashed horizontal line.

The flow over a rectangular urban area is presented in Case 2 (Figure 5b) and Case 3 (Figure 5c). As shown in Figure 5b, in Dome 1, only inflow (blue hollow arrows) appears, and the outflow is absent on the measured vertical plane along the long side. This phenomenon is consistent with that of the urban dome flow in a stale layer proposed by Fan et al. (2019c), according to which the outflows are perpendicular to the long side over a rectangular urban area with an aspect ratio of 4 (the ratio of the long side to short side). On the measured vertical plane, both inflow and outflow are observed (marked as red curved arrows) in Dome 2 of Case 2. The results of Case 3 in Figure 5c provide a perspective from another direction (view from the short side). Strong outflows (blue hollow arrows) in lower-level Dome 1 can be observed, meaning that the outflows of Dome 1 are perpendicular to the long sides. There are no obvious outflows in Dome 2. The shear region between Domes 1 and 2 does not exist either (Figure 5c), in contrast to Case 1 (Figure 5a). However, plumes are present, which connect Domes 1 and 2. These plumes enhance the heat and mass transfer between the two domes, which accelerates mixing. The results of Cases 2 and 3 indicate that the inflows and outflows lie on the same vertical plane along the long side direction in Dome 2, i.e. perpendicular to the short sides of the rectangle, which is different from those in Dome 1, where the inflows and outflows are located on different vertical planes.

Case 4 (Figure 5d, viewed from the side) and Case 5 (Figure 5e, viewed from the corner) demonstrate the flow over a square urban area from different viewpoints. Considering both Figure 5d and 5e, the flow in Dome 1 is characterised as a strong diagonal inflow (blue hollow arrows in Figure 5e) and side outflow (blue hollow arrows in Figure 5d), which agrees well with the results obtained in Fan et al. (2019c). As for the flow structures in Dome 2, both inflows and outflows (red curved arrows in Figure 5e) are present on the vertical plane aligned with the diagonal of the square city, whereas plumes appear on strong outflows on the vertical plane perpendicular to the edges (Case 4, Figure 5d).

Figure 5f displays the velocity field over a triangular city. Due to the shape of the triangle, both the flows over the corner (right part of the flow field) and the side region (left part) can be simultaneously observed. In the lower stable layer, Dome 1 presents both strong inflow (right part over the corner) and strong outflow (left part over the side). Similarly, plumes rise on the strong outflow from Dome 1 to Dome 2 on the left part over the side region of the triangular city. On the right part, both inflow and outflow (red curved arrow) appear on this viewed vertical plane in the neutral layer. The characteristics of the flow over the corner and side are observed on this single vertical plane.

In summary, the mean flow structure at the two-dome stage is considerably affected by the shapes of urban areas. In Dome 1 within the lower stable layer, the lower-level inflows are mainly present along the angular bisector across the corners and the outflows are perpendicular to the edges, which has the same characteristics as those of the urban dome flow in a completely stably stratified (no neutral layer) environment (Fan et al. 2019c). In Dome 2 within the upper neutral layer, the flow structures exhibit different trends. If the outflow of Dome 1 is strong on a specific vertical plane, the inflow of Dome 2 is less organised and the plumes rise from the outflow of Dome 1. In contrast, if the outflow of Dome 1 is weak, which is along the direction over the corners in our studied cases, the inflows of Dome 2 in the neutral layer is strong and organised. Meanwhile, the main outflow of Dome 2 would appear on the same vertical plane as that of the inflow, i.e. the vertical plane along the angular bisector across the corners.

3.1.2 Horizontal plane

To support the results presented in Section 3.1.1, the velocity fields on the horizontal planes were also measured. Only three cases (Cases 2, 4 and 6) are displayed in Figures 6-8 for the following reasons. The velocity fields over the circular urban area are symmetrical (Fan et al. 2018b, 2019c), and thus, not presented here for conciseness. Cases 2 and 3 have the same shape. Therefore, only Case 2 is shown here. Similarly, Case 4 is chosen out of the cases with square urban areas. The velocity field is also a result of 30-s average (900 images).

<Fig. 6>

<Fig. 7>

<Fig. 8>

Cases 2, 4 and 6 all present strong convergent inflows in Dome 1 (marked by white hollow arrows) along the angular bisector over the corner of the urban area in the near-surface region (Figures 6b-8b). Simultaneously, the strong divergent outflows in Dome 1 are perpendicular to the edges (Figures 6c-8c). The velocity field at the interface (z = 40 mm) between the lower stable layer and upper neutral layer is also obtained. As shown in Figures 6d-8d, both inflows over the corner and outflows over the sides are present at the top of the stable layer (or bottom of the neutral layer). The inflows observed at the interface belong to Dome 2 in the neutral layer aloft. Therefore, the inflows of Dome 2 are mainly present along the angular bisector over the corner, which supports the results for the vertical planes in Cases 1-6.

3.2 Turbulence statistics on the vertical plane

The turbulence statistics, including turbulent kinetic energy (TKE), momentum flux and turbulence production (P_{all}), were calculated based on the instantaneous velocity fields (30 Hz, 30 s) on vertical planes. Three turbulence-related parameters are analysed separately in the following three subsections.

3.2.1 TKE

TKE is calculated as $k = \left(\overline{u'^2} + \overline{w'^2}\right) \Big/ 2$ (m^2 s^{-2}), where u' and w' are the temporal fluctuations in the horizontal and vertical velocity components, respectively. The results are displayed in Figure 9.

<Fig. 9>

In all six cases, abnormally large TKEs are observed at the top left of the figures (marked by a blue curve), which are induced by interference from the laser light (Laser 1) reflection. This reflection is generated from the water surface and the wall of the water tank. We tried several methods to minimize the reflections, such as attaching a black non-reflective cloth to the inside of the water tank wall. This method did help to reduce the reflection from the wall. However, during the experiments, Laser 2 (Figure 2a) was also required to measure the velocity fields on the horizontal planes, and hence the wall of the water tank could not be blocked. The reflection from the water surface was unavoidable, as the water surface could not be obstructed to allow the view from Camera 2 (Figure 2a).

As shown in Figure 9a, b and e, the large-TKE regions are primarily present above the urban area, which is mainly generated by buoyancy. For the cases with strong side outflows in Dome 1 (Figure c, d and f), the large-TKE regions are also observed in the outflow regions besides the regions above the urban areas. This effect is presented more clearly in Case 6 (Figure 9f), i.e. the TKE is much larger on the left side of the urban area, due to the side outflow, than that on the right side. The plumes between Domes 1 and 2 can also be traced in TKE fields (Figure 9c–f) as those in the velocity fields in Figure 5c, d and f. The TKE fields in Figure 9 are also highly correlated with the velocity fields in Figure 5, indicating that a large mean velocity induces a large TKE.

3.2.2 Momentum flux

The momentum flux is defined as $\overline{u'w'}$ (m^2 s^{-2}) (Zou et al. 2017; Yin et al. 2019a), which is normalised with u_d^2, as shown in Figure 10.

<Fig. 10>

Momentum flux represents the characteristics of momentum transfer. Regions with

large positive (red) or negative (blue) momentum flux are marked in different cases for a clearer description and analysis. In this study, there are mainly two types of momentum transfer fields due to the different main mean flow directions, i.e. transfer of horizontal momentum in the vertical direction (Type 1) and that of vertical momentum in the horizontal direction (Type 2). Large areas of Types 1 and 2 momentum transfer are marked with solid and dashed white ellipses, respectively.

In Case 1 over a circular urban area (Figure 10a), six regions are marked, which contain two Type 1 regions (R3 and R6) and four Type 2 regions (R1, R2, R4 and R5). Regions R3 and R6 (Figure 10a) present a uniformly distributed momentum flux in the vertical direction and elongate in the horizontal direction, suggesting that both convergent inflow at the lower level (positive momentum transfer upward in R3 and negative momentum transfer upward in R6) and divergent outflow at the upper level (negative momentum transfer downward in R3 and positive momentum transfer downward in R6) in Dome 1 contribute to momentum transfer. The strong vertical movement (Type 2 regions), which results from the buoyancy, induces mixing and entrainment in the horizontal direction.

Figure 10b shows the contour map of momentum flux over a rectangular urban area viewed from the long side. Although the inflow and outflow of Dome 2 in the neutral layer are evident, the transfer of horizontal momentum in the vertical direction is not evident in these regions. The regions where strong momentum transfer occurs are all Type 2. Note that there are no extensive red or blue areas in R3. Instead, it is filled with many small areas of red or blue patches, showing a complicated momentum transfer pattern along the long side. If it is viewed from the short side of the rectangle (Case 3, Figure 10c), two obvious Type 2 regions are observed in Dome 1.

In Figure 10d, Type 1 regions (R3–R5) are mainly present in Dome 1, whereas Type 2 regions (R1 and R2) are primarily present in Dome 2. In regions R3–R5, the mean horizontal velocity is large due to the strong outflows of Dome 1 perpendicular to the edges. The momentum transfer is dominated by the downward transfer of negative momentum (R3 and R4, red patches) and positive momentum (R5, blue patches), which is different from Case 1 with both upward and downward transfer. In contrast, the mean velocity is mainly created by the convergent inflow across the corner in Case 5 (Figure 10e). Therefore, the two large areas of Type 1 regions in Figure 10e are generated by the upward transfer of positive momentum (R1, red patches) and negative momentum (R2, blue patches).

For the flow over the triangular urban area (Case 6, Figure 10f), the strong convergent inflow over the corner (right-hand side of the urban area) and divergent outflow over the side (left-hand side) appear on the same measured vertical plane. Therefore, both downward transfer (R3, red patches) of negative momentum and upward transfer (R4, blue patches) of negative momentum can be observed. Type 2 regions (R1 and R2) also present in Dome 2 due to strong upward motions.

3.2.3 Turbulence production

The turbulence production P_{all} (on the 2D plane) is defined as follows:

$$P_{all} = P_1 + P_2 + P_3 + P_4 = -\overline{u'u'}\frac{\partial \bar{u}}{\partial x} - \overline{u'w'}\frac{\partial \bar{u}}{\partial z} - \overline{u'w'}\frac{\partial \bar{w}}{\partial x} - \overline{w'w'}\frac{\partial \bar{w}}{\partial z} \quad (4)$$

where $P_1 = -\overline{u'u'}\frac{\partial \bar{u}}{\partial x}$, $P_2 = -\overline{u'w'}\frac{\partial \bar{u}}{\partial z}$, $P_3 = -\overline{u'w'}\frac{\partial \bar{w}}{\partial x}$ and $P_4 = -\overline{w'w'}\frac{\partial \bar{w}}{\partial z}$. $\bar{u}$ and $\bar{w}$ are the average horizontal and vertical velocity components, respectively, and x and z are the horizontal and vertical coordinates. The term (P_1+P_2) represents the energy transfer between the mean flow and TKE component induced by the horizontal velocity fluctuation ($\overline{u'^2}/2$). Similarly, the energy transfer between the mean flow and TKE component induced by the vertical velocity fluctuation ($\overline{w'^2}/2$) is expressed as (P_3+P_4) (Hudson et al. 1996). A positive term (P_1, P_2, P_3, P_4 or P_{all}) represents energy transfer from the mean flow to the TKE in that term. Otherwise, it implies that the mean flow extracts energy from turbulence fluctuations (Xia et al. 2003). In this study, the turbulence production (P_1, P_2, P_3, P_4 and P_{all}) is non-dimensionalised by the convective velocity scale u_d and length-scale hydraulic diameter d, to compare different cases (Yin et al. 2020). The non-dimensional turbulence production is expressed as $P_1^* = P_1 d / u_d^3$, $P_2^* = P_2 d / u_d^3$, $P_3^* = P_3 d / u_d^3$, $P_4^* = P_4 d / u_d^3$ and $P_{all}{}^* = P_{all} d / u_d^3$. The contour maps of turbulence production ($P_{all}{}^*$) are shown in Figure 11. The other terms ($P_1{}^*$ to $P_4{}^*$) are given in the Appendix.

<Fig. 11>

Turbulence is produced by shear and buoyancy. In Figures 11 and A1, red and blue colours represent positive and negative turbulence production, respectively. In all six cases, the overall turbulence production ($P_{all}{}^*$) in Dome 2 is largely determined by the fourth term $P_4{}^*$, indicating that the turbulent fluctuations are mainly induced by the vertical movement of buoyancy-driven flows. The turbulence production in Dome 1 is more complicated and different in various cases.

For the case with a circular urban area (Case 1, Figure 11a), the $P_{all}{}^*$ contour map can be divided into two regions (R1 and R2), which are dominated by positive (red) and negative (blue) values, respectively. According to the contour maps of individual terms, Dome 1 is affected by $P_1{}^*$(shear production, Figure A1(a,i)) and $P_4{}^*$(buoyancy production, Figure A1(a,iv)). In region R1, $P_1{}^*$ is negative, whereas $P_4{}^*$ is positive. In addition, $P_4{}^*$ is dominant, and finally, decides the sign of the $P_{all}{}^*$ contour map. The

opposite is the case for region R2.

In Case 2 (Figure 11b), the value of term P_4^* is much larger than those of the other terms and determines P_{all}^* in all three marked regions (R1–R3). If the flow is viewed from the short side (Case 3, Figure 11c), the turbulence production is determined by P_1^* and P_4^*, with P_4^* being dominant in regions R1 and R2 (Figure 11c). Besides P_4^*, P_2^* also plays a role in the region of strong side outflow (R4), indicating the relative importance of normal stress in the horizontal direction.

As shown in Figure 11d, the overall production is characterised by the production of the horizontal velocity fluctuation components (P_1^* and P_2^*) in the strong side outflow region (R4). In all three regions (R1, R2 and R4) of Dome 1, strong influences of the term P_1^* appear, suggesting the importance of shear production. As for the production map over a square urban area viewed from the corner (Case 5, Figure 11e), it is similar to that in Case 2 (viewed as rectangular from the long side), where P_4^* dominates the overall production. Because the strong inflow across the corner and side outflow can be viewed on the same vertical plane over the triangular urban area, P_1^* is found to be important in Dome 1 (regions R1 and R2), as shown in Figure 11f.

Overall, the turbulence production is dominated by P_4^* over the urban area in both Domes 1 and 2, whereas P_1^* plays an important role over the rural area, especially in the region of strong side outflows. This phenomenon is consistent with the theoretical analysis conducted in Fan et al. (2017a), where the turbulent structure is dominated by shear over the outer part of the urban area and by the plume near the urban centre.

4. Discussion

There are both similarities and differences between the conditions with and without a neutral layer aloft. In both conditions, the urban heat dome flow near the surface within the stable layer is characterised as the convergent inflow along the angular bisector and divergent outflow perpendicular to the sides. The main difference between the two conditions is that the urban heat dome flow can penetrate the stable layer and induce a second circulating flow in the neutral layer if the stable layer is thin enough in the case of neutral layer aloft, which will enhance the turbulent heat and mass transfer in the stable and neutral layers. At the two-dome stage, the urban dome flow in the near-surface stable layer (Dome 1) induces a second dome (Dome 2) in the neutral layer aloft, both of which are affected significantly by the shape of underlying urban areas. According to the linearised small-perturbation model (Chun 1995; Baik et al. 2007; Vukovich 1971; Fan et al. 2017b), Dome 2 can be induced by the perturbation of Dome 1 and internal gravity waves. In contrast, the intermittently rising strong thermals from Dome 1 can penetrate the above neutral layer, and thus, create a low-pressure region, inducing a convergent inflow in Dome 2. A shear layer is formed between the convergent inflow in Dome 2 and the divergent outflow of Dome 1 (Fan et al. 2019a). The shear layer between Domes 1 and 2 limits the heat

and mass transfer between them. Although the excess heat (urban–rural difference) in Dome 2 is much smaller than that in Dome 1 (Fan et al. 2019a), the mean speed in Dome 2 has a similar magnitude to that in Dome 1 due to the neutral environment (Hidalgo et al. 2008a, 2010; Lemonsu and Masson 2002). This Dome 1-induced elevated Dome 2 in the neutral layer is important for the pollutant redistribution, high-level cloud formation, elevated convection (Corfidi et al. 2008) and safety of aviation. Besides the convective flow in the atmosphere, this two-dome flow structure can appear in ocean convection (MacKinnon 2013) and industrial applications, such as thermal energy storage (TES) tanks (Zurigat et al. 1991; Moreno et al. 2014).

Our study has several limitations. First, complicated topography, such as valleys, basins or mountains, is not considered, which can have a substantial influence on inversion breakup (Whiteman and McKee 1982; Colette et al. 2003; Rendón et al. 2015). Second, the rural area in this study is not heated up. If the rural area is also heated up, the mean horizontal speed in Dome 1 may increase due to the less stable conditions and the convective turbulence structures may alter the characteristics of the outflow of Dome 1 (Ryu et al. 2013; Hidalgo et al. 2008a). Third, the roughness is not simulated. The influences of roughness on the overall structure of the urban dome flow are small and neglected compared to the heat flux and stable stratification (Lu et al. 1997b; Hildebrand and Ackerman 1984; Vukovich and Dunn 1978; Fan et al. 2019c). However, if the buildings are sufficiently high (high-rise buildings) and penetrate the neutral layer, the mixing between Domes 1 and 2 can be substantially enhanced and the flow speed in Dome 2 can be considerably increased. Note that the wind and thermal environment in the urban canopy layer is substantially affected by roughness, such as buildings (Fan et al. 2016a; Hang et al. 2018; Zhang et al. 2019; Yin et al. 2018, 2019b; Chen et al. 2017). Moreover, the density profile in the current setup is SBI. An EI case is worth investigating. The influences of various heat flux, stable layer height, stability and neutral layer height could also be further studied in future experiments.

5. Conclusions

Inversion breakup plays a crucial role in heat and mass transfer in the atmospheric boundary layer, which considerably affects the pollutant concentration at the pedestrian level. The characteristics of inversion breakup at the two-dome stage over various shapes of urban areas are investigated and summarised as follows.

The mean flow structures in both Domes 1 and 2 are substantially affected by urban shape. The characteristics of the angular bisector convergent inflow and the side divergent outflow perpendicular to the edges in Dome 1 are the same as the urban dome flow in a completely stable and stratified environment without a neutral layer aloft. The convergent inflow of Dome 2 near the interface between the stable and neutral layers has the same direction as that of Dome 1, which is mainly along the angular bisector across the corners of urban areas. However, the divergent outflow in Dome 2 does not exhibit the side outflow effect, and instead is present on the same vertical plane of the

Dome 2 inflow, i.e. along the angular bisector across the corner.

Positions of large mean velocity also present large TKE values, indicating that a large mean speed is accompanied by large velocity fluctuations. Near the urban centre, the flow is dominated by thermal plume structures with strong buoyancy and induces transfer of vertical momentum in the horizontal direction (Type 2). In the urban periphery or rural area, the horizontal velocity component is large and produces more transfer of horizontal momentum in the vertical direction (Type 1). This Type 1 momentum flux is more evident in the strong outflow regions perpendicular to the urban edges. Besides the large horizontal velocity, the plumes also grow along the strong outflow regions, which increases mixing between Domes 1 and 2. The characteristics of turbulence production in Domes 1 and 2 are different. The turbulence production is dominated by the term P_4 in Dome 2, which is induced by buoyancy. Both P_1 (shear) and P_4 (buoyancy) are important in Dome 1, whereas P_3 is negligible in all cases.

Acknowledgement

This project was financially supported by a grant from the National Natural Science Foundation of China (51778555) and (51908489).

References

Allen, M. and Holmes, B. (2015). Seasonal and diurnal patterns of temperature inversion formation and breakup in a topographically complex urban environment. *National Conference on Undergraduate Research*, Cheney WA, USA.

Baik, J.-J., Kim, Y.-H., Kim, J.-J. and Han, J.-Y. (2007). Effects of boundary-layer stability on urban heat island-induced circulation. *Theor Appl Climatol* 89(1-2): 73-81.

Bornstein, R. D. (1968). Observations of the urban heat island effect in New York City. *J Appl Meteorol* 7(4): 575-582.

Cenedese, A. and Monti, P. (2003). Interaction between an inland urban heat island and a sea-breeze flow: A laboratory study. *J Appl Meteorol* 42(11): 1569-1583.

Chen, L., Hang, J., Sandberg, M., Claesson, L., Di Sabatino, S. and Wigo, H. (2017). The impacts of building height variations and building packing densities on flow adjustment and city breathability in idealized urban models. *Build Environ* 118: 344-361.

Chen, Z., Chen, D., Zhao, C., Kwan, M. P., Cai, J., Zhuang, Y., Zhao, B., Wang, X., Chen, B., Yang, J., Li, R., He, B., Gao, B., Wang, K. and Xu, B. (2020). Influence of meteorological conditions on $PM_{2.5}$ concentrations across China: A review of methodology and mechanism. *Environ Int* 139: 105558.

Christen, A., Bernhofer, C., Parlow, E., Rotach, M. W. and Vogt, R. (2003). Partitioning of turbulent fluxes over different urban surfaces. *Fifth International Conference on*

Urban Climate, Lodz, Poland .

Chun, H.-Y. (1995). Enhanced response of a stably stratified two-layer atmosphere to low-level heating. *J Meteorol Soc Jpn* 73(3): 685-696.

Clements, C. B., Whiteman, C. D. and Horel, J. D. (2003). Cold-air-pool structure and evolution in a mountain basin: Peter Sinks, Utah. *J Appl Meteorol* 42(6): 752-768.

Colette, A., Chow, F. K. and Street, R. L. (2003). A numerical study of inversion-layer breakup and the effects of topographic shading in idealized valleys. *J Appl Meteorol* 42(9): 1255-1272.

Colomer, J., Boubnov, B. and Fernando, H.J.S. (1999). Turbulent convection from isolated sources. *Dynam Atmos Oceans* 30(2): 125-148.

Corfidi, S. F., Corfidi, S. J. and Schultz, D. M. (2008). Elevated convection and castellanus: Ambiguities, significance, and questions. *Weather Forecast* 23(6): 1280-1303.

Czarnecka, M. and Nidzgorska-Lencewicz, J. (2017). The impact of thermal inversion on the variability of PM_{10} concentration in winter seasons in Tricity. *Environ Prot Eng* 43(2): 157-172.

Deosthali, V. (2000). Impact of rapid urban growth on heat and moisture islands in Pune City, India. *Atmos Environ* 34(17): 2745-2754.

Evans, R. B. (1979). *The Contribution of Ozone Aloft to Surface Ozone Maxima*. Ph.D. thesis, University of North Carolina, Chapel Hill.

Fan, Y., Hunt, J. C. R., Wang, Q., Yin, S. and Li, Y. (2019a). Water tank modelling of variations in inversion breakup over a circular city. *Build Environ* 164: 106342.

Fan, Y., Hunt, J. C. R., Yin, S. and Li, Y. (2019b). Mean shear flow in recirculating turbulent urban convection and the plume-puff eddy structure below stably stratified inversion layers. *Theor Appl Climatol* 135(3): 1485-1499.

Fan, Y., Hunt, J. C. R. and Li, Y. (2017a). Buoyancy and turbulence-driven atmospheric circulation over urban areas. *J Environ Sci* 59: 63-71.

Fan, Y., Li, Y., Bejan, A., Wang, Y. and Yang, X. (2017b). Horizontal extent of the urban heat dome flow. *Sci Rep-UK* 7(1): 11681.

Fan, Y., Li, Y., Hang, J., Wang, K. and Yang, X. (2016a). Natural convection flows along a 16-storey high-rise building. *Build Environ* 107: 215-225.

Fan, Y., Li, Y., Wang, X. and Catalano, F. (2016b). A new convective velocity scale for studying diurnal urban heat island circulation. *J Appl Meteorol Clim* 55: 2151–2164.

Fan, Y., Li, Y. and Yin, S. (2018a). Interaction of multiple urban heat island circulations under idealised settings. *Build Environ* 134: 10-20.

Fan, Y., Li, Y. and Yin, S. (2018b). Non-uniform ground-level wind patterns in a heat

dome over a uniformly heated non-circular city. *Int J Heat Mass Tran* 124: 233-246.

Fan, Y., Wang, Q., Ge, J. and Li, Y. (2020). Conditions for transition from a plume to a dome above a heated horizontal area. *Int J Heat Mass Tran* 156: 119868.

Fan, Y., Wang, Q., Yin, S. and Li, Y. (2019c). Effect of city shape on urban wind patterns and convective heat transfer in calm and stable background conditions. *Build Environ* 162: 106288.

Fernando, H. J. S. (1987). The formation of a layered structure when a stable salinity gradient is heated from below. *J Fluid Mech* 182: 525-541.

Founda, D. and Santamouris, M. (2017). Synergies between urban heat island and heat waves in Athens (Greece), during an extremely hot summer (2012). *Sci Rep-UK* 7(1): 10973.

Godowitch, J. M., Ching, J. K. S. and Clarke, J. F. (1985). Evolution of the Nocturnal Inversion Layer at an Urban and Nonurban Location. *J Appl Meteorol Clim* 24(8): 791-804.

Hang, J., Luo, Z., Wang, X., He, L., Wang, B. and Zhu, W. (2017). The influence of street layouts and viaduct settings on daily carbon monoxide exposure and intake fraction in idealized urban canyons. *Environ Pollut* 220: 72-86.

Hang, J., Xian, Z., Wang, D., Mak, C. M., Wang, B. and Fan, Y. (2018). The impacts of viaduct settings and street aspect ratios on personal intake fraction in three-dimensional urban-like geometries. *Build Environ* 143: 138-162.

Hao, L., Huang, X., Qin, M., Liu, Y., Li, W. and Sun, G. (2018). Ecohydrological processes explain urban dry island effects in a wet region, Southern China. *Water Resour Res* 54(9): 6757-6771.

Hidalgo, J., Masson, V. and Gimeno, L. (2010). Scaling the daytime urban heat island and urban-breeze circulation. *J Appl Meteorol Clim* 49(5): 889-901.

Hidalgo, J., Masson, V. and Pigeon, G. (2008a). Urban-breeze circulation during the CAPITOUL experiment: numerical simulations. *Meteorol Atmos Phys* 102(3-4): 243-262.

Hidalgo, J., Pigeon, G. and Masson, V. (2008b). Urban-breeze circulation during the CAPITOUL experiment: observational data analysis approach. *Meteorol Atmos Phys* 102(3-4): 223-241.

Hildebrand, P. H. and Ackerman, B. (1984). Urban effects on the convective boundary layer. *J Atmos Sci* 41(1): 76-91.

Hoyos, C. D., Herrera-Mejia, L., Roldan-Henao, N. and Isaza, A. (2019). Effects of fireworks on particulate matter concentration in a narrow valley: the case of the Medellin metropolitan area. *Environ Monit Assess* 192(1): 6.

Huang, X., Cai, Y. and Li, J. (2019). Evidence of the mitigated urban particulate matter

island (UPI) effect in China during 2000-2015. *Sci Total Environ* 660: 1327-1337.

Hudson, J. D., Dykhno, L. and Hanratty, T. J. (1996). Turbulence production in flow over a wavy wall. *Exp Fluids* 20(4): 257-265.

Hunt, J. C. R., Richards, K. and Brighton, P. (1988). Stably stratified shear flow over low hills. *Q J Roy Meteor Soc* 114(482): 859-886.

Idso, C. D., Idso, S. B. and Balling Jr, R. C. (2013). The urban CO_2 dome of Phoenix, Arizona. *Phys Geogr* 19(2): 95-108.

Idso, C. D., Idso, S. B. and Balling, R. C. (2001). An intensive two-week study of an urban CO2 dome in Phoenix, Arizona, USA. *Atmos Environ* 35(6): 995-1000.

Jacobson, M. Z. (2010). Enhancement of local air pollution by urban CO_2 domes. *Environ Sci Technol* 44(7): 2497-2502.

Janhäll, S., Olofson, K. F. G., Andersson, P. U., Pettersson, J. B. and Hallquist, M. (2006). Evolution of the urban aerosol during winter temperature inversion episodes. *Atmos Environ* 40(28): 5355-5366.

Khalesi, B. and Mansouri Daneshvar, M. R. (2020). Comprehensive temporal analysis of temperature inversions across urban atmospheric boundary layer of Tehran within 2014–2018. *Modeling Earth Systems and Environment* 6(2): 967-982.

Krüger, E. and Emmanuel, R. (2013). Accounting for atmospheric stability conditions in urban heat island studies: the case of Glasgow, UK. *Landscape Urban Plan* 117: 112-121.

Largeron, Y. and Staquet, C. (2016). Persistent inversion dynamics and wintertime PM_{10} air pollution in Alpine valleys. *Atmos Environ* 135: 92-108.

Lemonsu, A. and Masson, V. (2002). Simulation of a summer urban breeze over Paris. *Bound-lay Meteorol* 104(3): 463-490.

Leukauf, D., Gohm, A. and Rotach, M. W. (2016). Quantifying horizontal and vertical tracer mass fluxes in an idealized valley during daytime. *Atmos Chem Phys* 16(20): 13049-13066.

Leukauf, D., Gohm, A., Rotach, M. W. and Wagner, J. S. (2015). The impact of the temperature inversion breakup on the exchange of heat and mass in an idealized valley: Sensitivity to the radiative forcing. *J Appl Meteorol Clim* 54(11): 2199-2216.

Li, H., Meier, F., Lee, X., Chakraborty, T., Liu, J., Schaap, M. and Sodoudi, S. (2018). Interaction between urban heat island and urban pollution island during summer in Berlin. *Sci Total Environ* 636: 818-828.

Li, J., Chen, H., Li, Z., Wang, P., Fan, X., He, W. and Zhang, J. (2019). Analysis of low-level temperature inversions and their effects on aerosols in the lower atmosphere. *Adv Atmos Sci* 36(11): 1235-1250.

Lindén, J. (2011). Nocturnal cool island in the Sahelian city of Ouagadougou, Burkina

Faso. *Int J Climatol* 31(4): 605-620.

Lokoshchenko, M. A. (2017). Urban heat island and urban dry island in Moscow and their centennial changes. *J Appl Meteorol Clim* 56(10): 2729-2745.

Lu, J., Arya, S. P., Snyder, W. H. and Lawson Jr, R. E. (1997a). A laboratory study of the urban heat island in a calm and stably stratified environment. Part I: Temperature field. *J Appl Meteorol* 36(10): 1377-1391.

Lu, J., Arya, S. P., Snyder, W. H. and Lawson Jr, R. E. (1997b). A laboratory study of the urban heat island in a calm and stably stratified environment. Part II: Velocity field. *J Appl Meteorol* 36(10): 1392-1402.

MacKinnon, J. (2013). Mountain waves in the deep ocean. *Nature* 501: 321.

Megaw, W. (1977). Thin layer brown haze. *J Aerosol Sci* 8(1): 21-29.

Moreno, P., Castell, A., Solé, C., Zsembinszki, G. and Cabeza, L. F. (2014). PCM thermal energy storage tanks in heat pump system for space cooling. *Energ Buildings* 82: 399-405.

Oke, T. R. (1973). City size and the urban heat island. *Atmos Environ* 7(8): 769-779.

Oke, T. R., Spronken-Smith, R., Jauregui, E. and Grimmond, C. (1999). The energy balance of central Mexico City during the dry season. *Atmos Environ* 33(24): 3919-3930.

Osthoff, H. D., Odame-Ankrah, C. A., Taha, Y. M., Tokarek, T. W., Schiller, C. L., Haga, D., Jones, K. and Vingarzan, R. (2018). Low levels of nitryl chloride at ground level: nocturnal nitrogen oxides in the Lower Fraser Valley of British Columbia. *Atmos Chem Phys* 18(9): 6293-6315.

Palarz, A., Celiński-Mysław, D. and Ustrnul, Z. (2019). Temporal and spatial variability of elevated inversions over Europe based on ERA-Interim reanalysis. *Int J Climatol* 40(3): 1335-1347.

Peters, L. K. (1975). On the criteria for the occurrence of fumigation inland from a large lake. *Atmos Environ (1967)* 9(9): 809-816.

Princevac, M. and Fernando, H. (2008). Morning breakup of cold pools in complex terrain. *J Fluid Mech* 616: 99-109.

Rasul, A., Balzter, H., Smith, C., Remedios, J., Adamu, B., Sobrino, J. A., Srivanit, M. and Weng, Q. (2017). A review on remote sensing of urban heat and cool islands. *Land* 6(2): 38.

Rendón, A. M., Salazar, J. F., Palacio, C. A. and Wirth, V. (2015). Temperature inversion breakup with impacts on air quality in urban valleys influenced by topographic shading. *J Appl Meteorol Clim* 54(2): 302-321.

Reuten, C. (2006). *Scaling and kinematics of daytime slope flow systems*, Ph.D. thesis, University of British Columbia.

Ryu, Y. H., Baik, J. J. and Han, J. Y. (2013). Daytime urban breeze circulation and its interaction with convective cells. *Q J Roy Meteor Soc* 139: 401-413.

Snyder, D. C., Dallmann, T. R., Schauer, J. J., Holloway, T., Kleeman, M. J., Geller, M. D. and Sioutas, C. (2008). Direct observation of the break-up of a nocturnal inversion layer using elemental mercury as a tracer. *Geophys Res Lett* 35(17): L17812.

Stull, R. B. (1988). *An Introduction to Boundary Layer Meteorology*, Kluwer Academic Publishers, Netherlands, Springer.

Tham, Y. J., Wang, Z., Li, Q., Yun, H., Wang, W., Wang, X., Xue, L., Lu, K., Ma, N. and Bohn, B. (2016). Significant concentrations of nitryl chloride sustained in the morning: investigations of the causes and impacts on ozone production in a polluted region of northern China. *Atmos Chem Phys*16(23): 14959-14977.

Vukovich, F. M. (1971). Theoretical analysis of the effect of mean wind and stability on a heat island circulation characteristic of an urban complex. *Mon Weather Rev* 99(12): 919-926.

Vukovich, F. M. and Dunn, J. (1978). A theoretical study of the St. Louis heat island: Some parameter variations. *J Appl Meteorol* 17(11): 1585-1594.

Wang, Q., Sun, Y., Xu, W., Du, W., Zhou, L., Tang, G., Chen, C., Cheng, X., Zhao, X. and Ji, D. (2018). Vertically resolved characteristics of air pollution during two severe winter haze episodes in urban Beijing, China. *Atmos Chem Phys* 18(4): 2495-2509.

Wang, X. and Gong, Y. (2010). The impact of an urban dry island on the summer heat wave and sultry weather in Beijing City. *Chin Sci Bull* 55(16): 1657-1661.

Wang, Z., Song, J., Chan, P. W. and Li, Y. (2020). The urban moisture island phenomenon and its mechanisms in a high-rise high-density city. *Int J Climatol* https://doi.org/10.1002/joc.6672.

Weston, M. J., Temimi, M., Nelli, N. R., Fonseca, R. M., Thota, M. S. and Valappil, V. K. (2020). On the analysis of the low-level double temperature inversion over the United Arab Emirates: a case study during April 2019. *IEEE Geosci Remote S*: 1-5 doi: 10.1109/LGRS.2020.2972597.

Whiteman, C. D. (1982). Breakup of temperature inversions in deep mountain valleys: Part I. Observations. *J Appl Meteorol* 21(3): 270-289.

Whiteman, C. D. and McKee, T. B. (1982). Breakup of temperature inversions in deep mountain valleys: Part II. Thermodynamic model. *J Appl Meteorol* 21(3): 290-302.

Willis, G. and Deardorff, J. (1974). A laboratory model of the unstable planetary boundary layer. *J Atmos Sci* 31(5): 1297-1307.

Xia, K.-Q., Sun, C. and Zhou, S.-Q. (2003). Particle image velocimetry measurement of the velocity field in turbulent thermal convection. *Phys Rev E* 68(6): 066303.

Xuan, J. and Zhang, B. (1999). A laboratory simulation of pollutant transportation over

a complex terrain. *Acta Meteorol Sin* 49(1): 85-90.

Yang, X., Li, Y., Luo, Z. and Chan, P. W. (2016). The urban cool island phenomenon in a high-rise high-density city and its mechanisms. *Int J Climatol* 37: 890-904.

Yin, S., Fan, Y., Li, Y., Sandberg, M. and Lam, K.-M. (2020). Experimental study of thermal plumes generated by a cluster of high-rise compact buildings under moderate background wind conditions. *Build Environ* Pre-proof: 107076.

Yin, S., Fan, Y., Sandberg, M. and Li, Y. (2019a). PIV based POD analysis of coherent structures in flow patterns generated by triple interacting buoyant plumes. *Build Environ* 158: 165-181.

Yin, S., Li, Y., Fan, Y. and Sandberg, M. (2018). Unsteady large-scale flow patterns and dynamic vortex movement in near-field triple buoyant plumes. *Build Environ* 142: 288-300.

Yin, S., Li, Y., Fan, Y. and Sandberg, M. (2019b). Experimental investigation of near-field stream-wise flow development and spatial structure in triple buoyant plumes. *Build Environ* 149: 79-89.

Zhang, B. and Sang, J. (1999). Experimental and numerical modeling of plume dispersion in stratified atmospheres. *Chin. J. Atmos. Sci.* 23(1): 19-24.

Zhang, B. and Sang, J. (2004). The assessment of atmospheric environment and experimental fluid dynamics in cities and industrial areas-simulation studies of wind environment II. *Mechanics and Engineering* 26(4): 1-6.

Zhang, K., Chen, G., Wang, X., Liu, S., Mak, C. M., Fan, Y. and Hang, J. (2019). Numerical evaluations of urban design technique to reduce vehicular personal intake fraction in deep street canyons. *Sci Total Environ* 653: 968-994.

Zou, J., Zhou, B. and Sun, J. (2017). Impact of eddy characteristics on turbulent heat and momentum fluxes in the urban roughness sublayer. *Bound-lay Meteorol* 164(1): 39-62.

Zurigat, Y. H., Liche, P. R. and Ghajar, A. J. (1991). Influence of inlet geometry on mixing in thermocline thermal energy storage. *Int J Heat Mass Tran* 34(1): 115-125.

Appendix

The non-dimensional turbulence production terms (P_1^* to P_4^*).

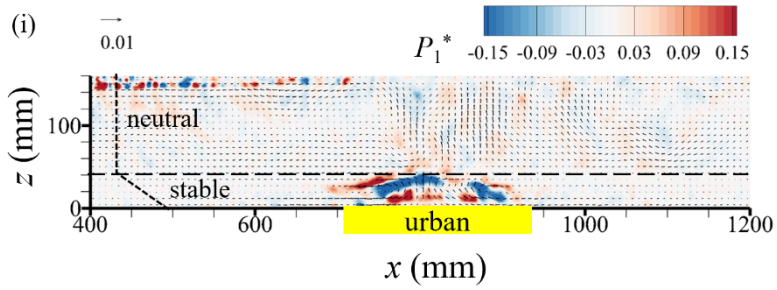
(i)
0.01
P_1^*
-0.15 -0.09 -0.03 0.03 0.09 0.15
neutral
stable
urban
z (mm)
x (mm)

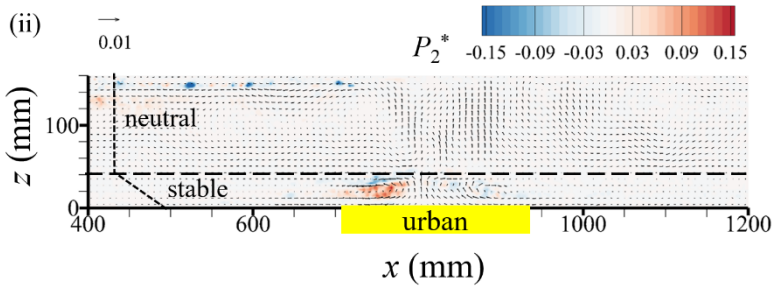
(ii)
0.01
P_2^*
-0.15 -0.09 -0.03 0.03 0.09 0.15
neutral
stable
urban
z (mm)
x (mm)

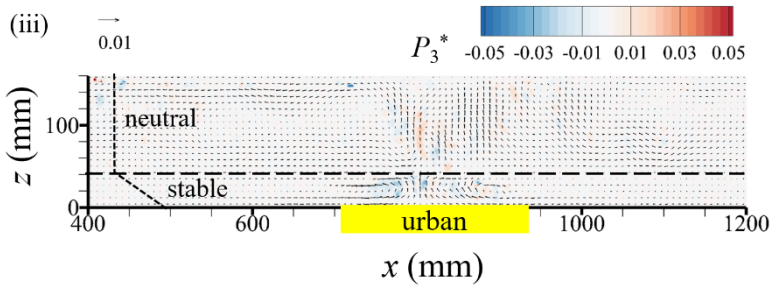
(iii)
0.01
P_3^*
-0.05 -0.03 -0.01 0.01 0.03 0.05
neutral
stable
urban
z (mm)
x (mm)

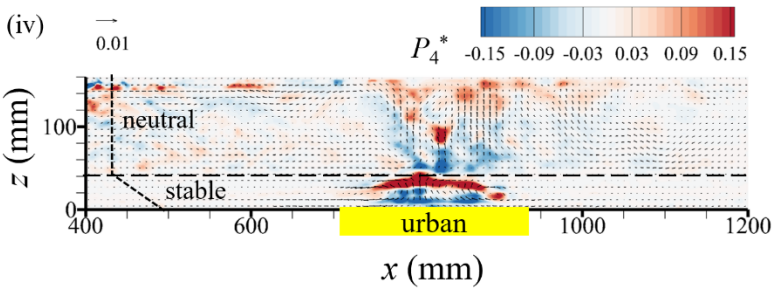
(iv)
0.01
P_4^*
-0.15 -0.09 -0.03 0.03 0.09 0.15
neutral
stable
urban
z (mm)
x (mm)

(a)

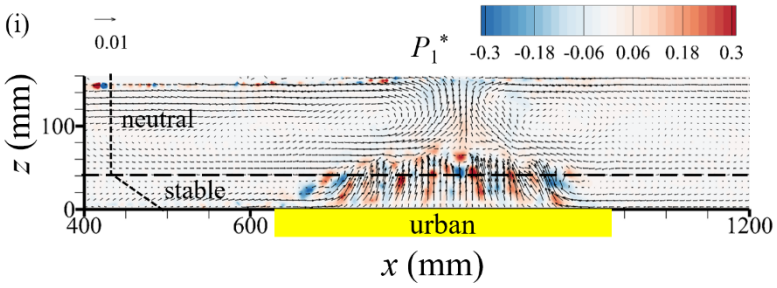
(i)
0.01
P_1^*
-0.3 -0.18 -0.06 0.06 0.18 0.3
neutral
stable
urban
z (mm)
x (mm)

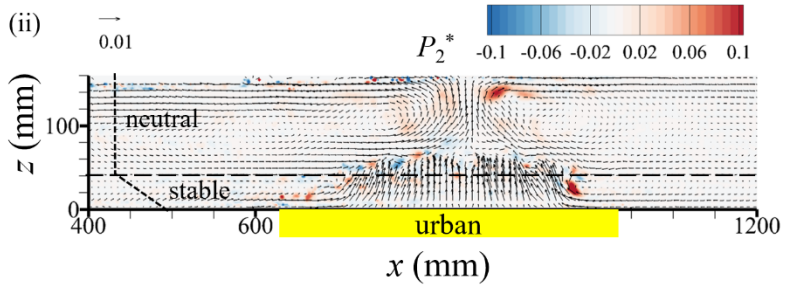
(ii)
0.01
P_2^*
-0.1 -0.06 -0.02 0.02 0.06 0.1
z (mm)
100
0
neutral
stable
400
600
urban
1200
x (mm)

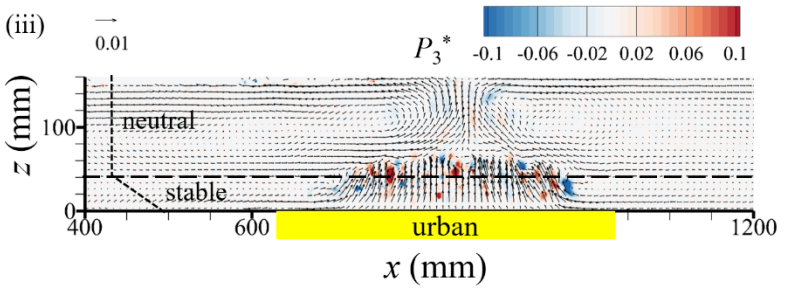
(iii)
0.01
P_3^*
-0.1 -0.06 -0.02 0.02 0.06 0.1
z (mm)
100
0
neutral
stable
400
600
urban
1200
x (mm)

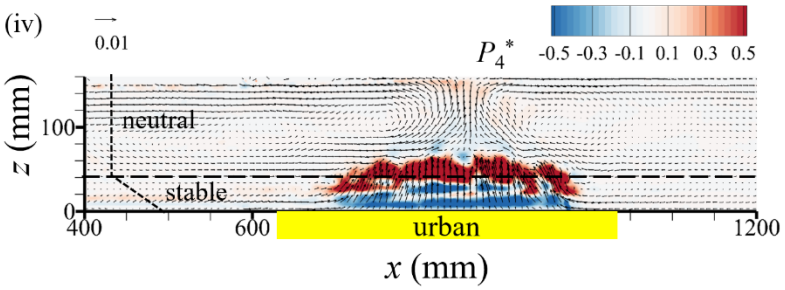
(iv)
0.01
P_4^*
-0.5 -0.3 -0.1 0.1 0.3 0.5
z (mm)
100
0
neutral
stable
400
600
urban
1200
x (mm)

(b)

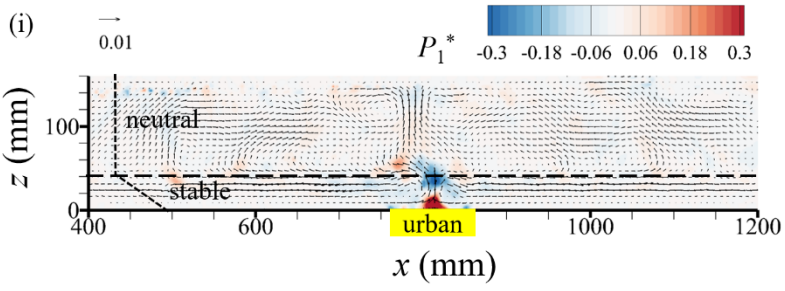
(i)
0.01
P_1^*
-0.3 -0.18 -0.06 0.06 0.18 0.3
z (mm)
100
0
neutral
stable
400
600
urban
1000
1200
x (mm)

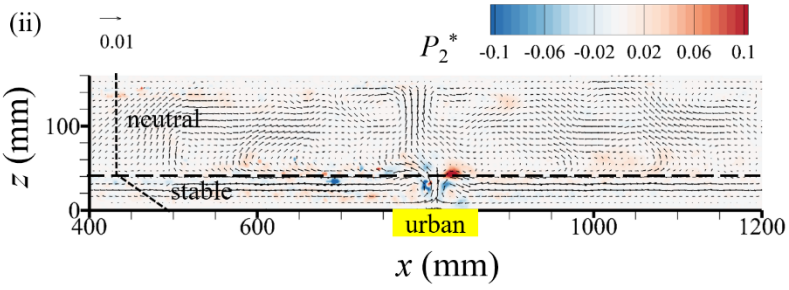
(ii)
0.01
P_2^*
-0.1 -0.06 -0.02 0.02 0.06 0.1
z (mm)
100
0
neutral
stable
400
600
urban
1000
1200
x (mm)

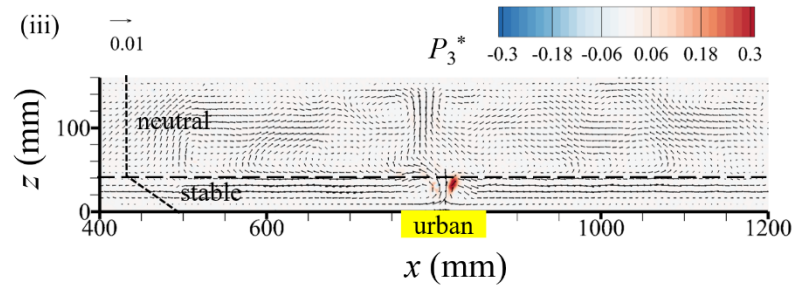
(iii)
0.01
P_3^*
-0.3 -0.18 -0.06 0.06 0.18 0.3
neutral
stable
urban
z (mm)
100
0
400
600
1000
1200
x (mm)

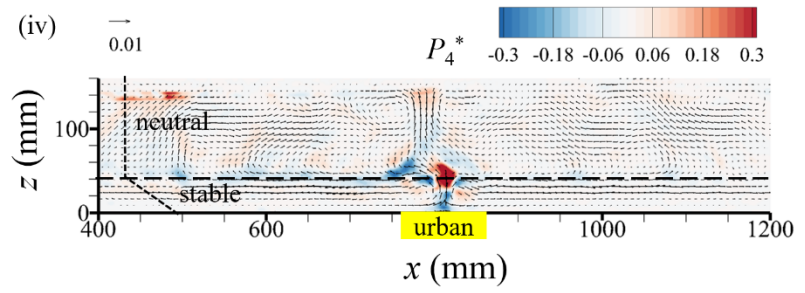
(iv)
0.01
P_4^*
-0.3 -0.18 -0.06 0.06 0.18 0.3
neutral
stable
urban
z (mm)
100
0
400
600
1000
1200
x (mm)

(c)

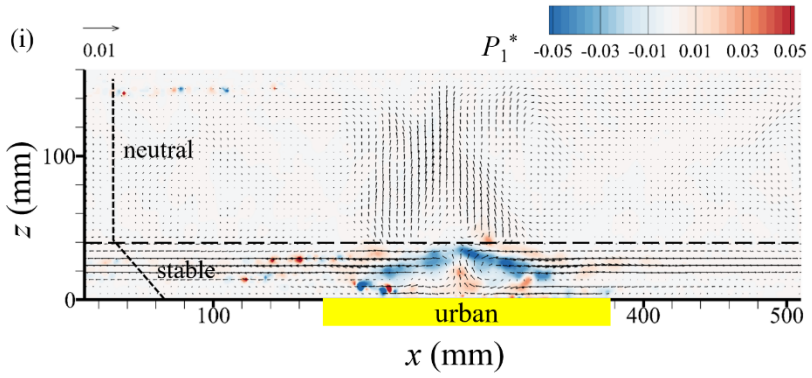
(i)
0.01
P_1^*
-0.05 -0.03 -0.01 0.01 0.03 0.05
neutral
stable
urban
z (mm)
100
0
100
400
500
x (mm)

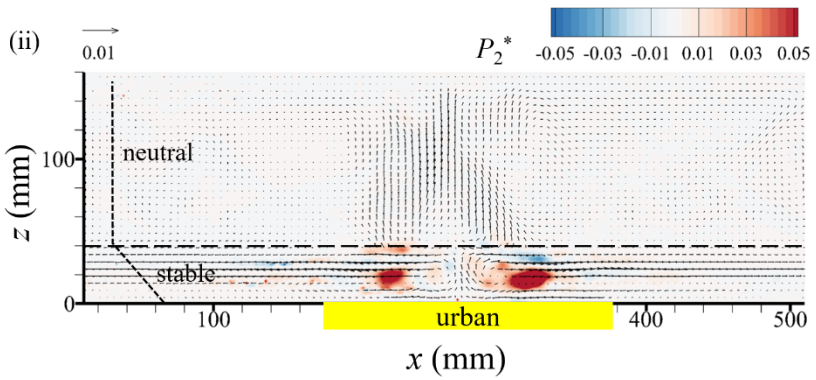
(ii)
0.01
P_2^*
-0.05 -0.03 -0.01 0.01 0.03 0.05
neutral
stable
urban
z (mm)
100
0
100
400
500
x (mm)

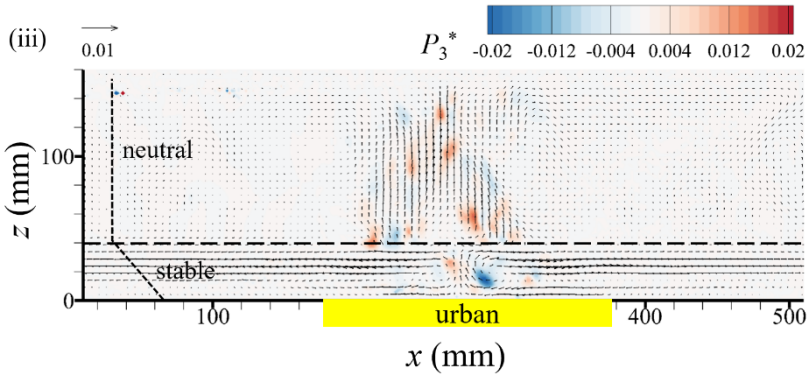
(iii)
0.01
P_3^*
-0.02 -0.012 -0.004 0.004 0.012 0.02
neutral
stable
urban
z (mm)
x (mm)
0
100
400
500

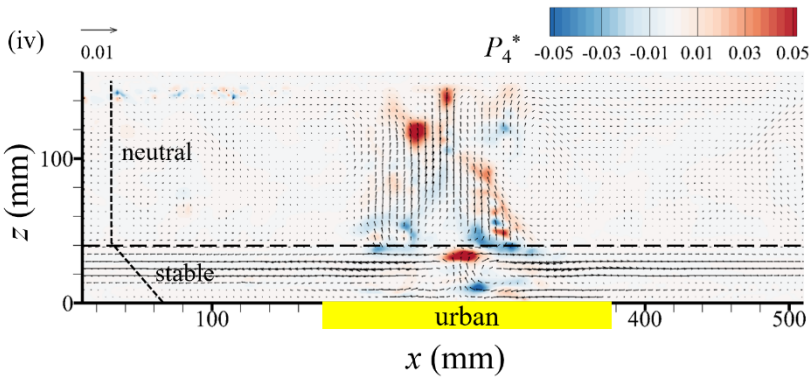
(iv)
0.01
P_4^*
-0.05 -0.03 -0.01 0.01 0.03 0.05
neutral
stable
urban
z (mm)
x (mm)
0
100
400
500

(d)

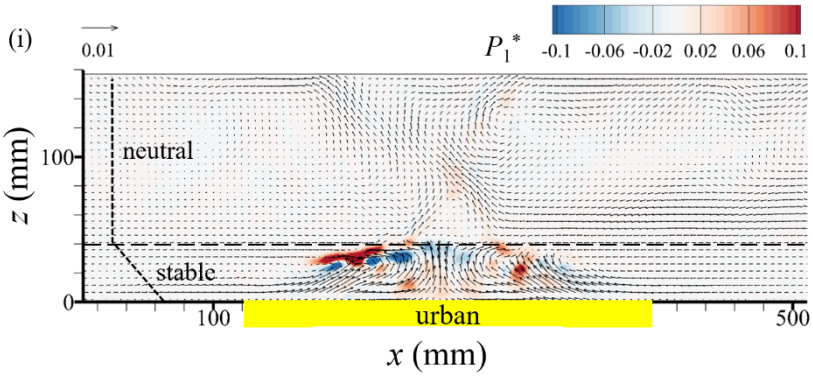
(i)
0.01
P_1^*
-0.1 -0.06 -0.02 0.02 0.06 0.1
neutral
stable
urban
z (mm)
x (mm)
0
100
500

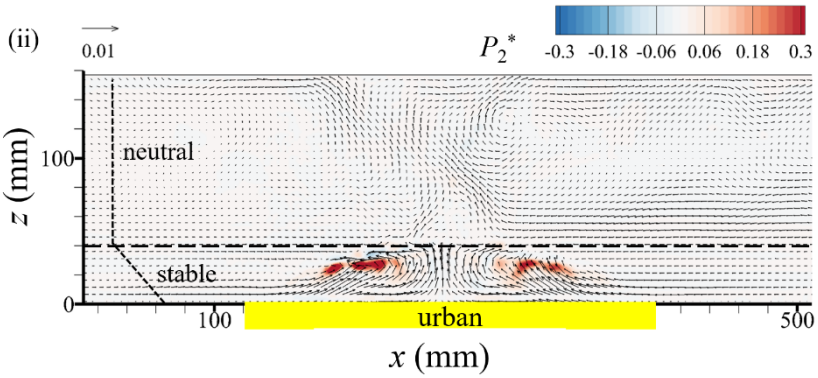
(ii)
0.01
P_2^*
-0.3 -0.18 -0.06 0.06 0.18 0.3
neutral
stable
urban
z (mm)
x (mm)
0
100
500

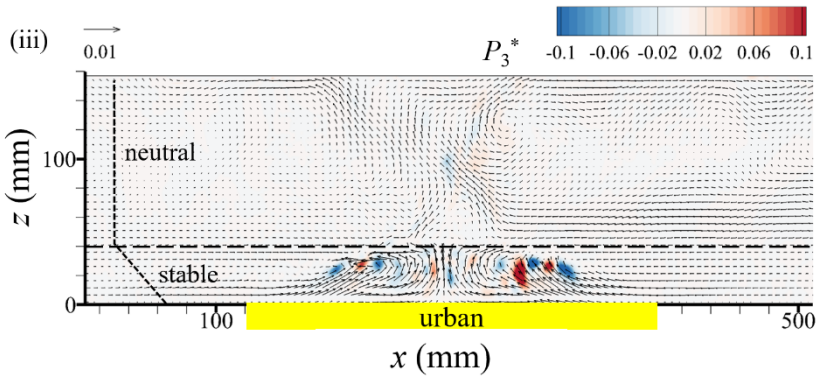
(iii)
0.01
P_3^*
-0.1 -0.06 -0.02 0.02 0.06 0.1
neutral
stable
urban
100
0
100
500
z (mm)
x (mm)

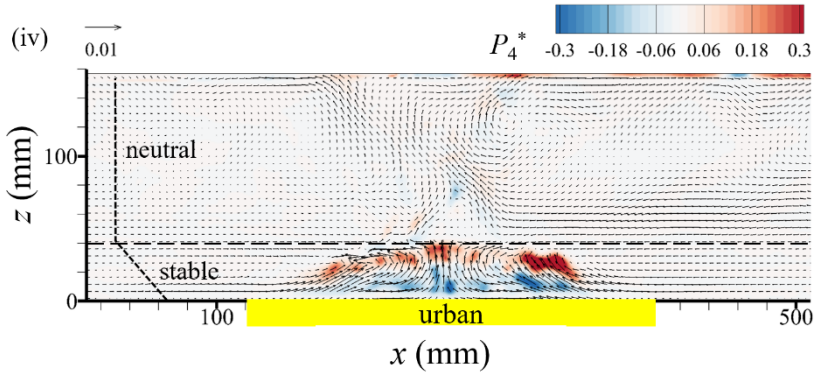
(iv)
0.01
P_4^*
-0.3 -0.18 -0.06 0.06 0.18 0.3
neutral
stable
urban
100
0
100
500
z (mm)
x (mm)

(e)

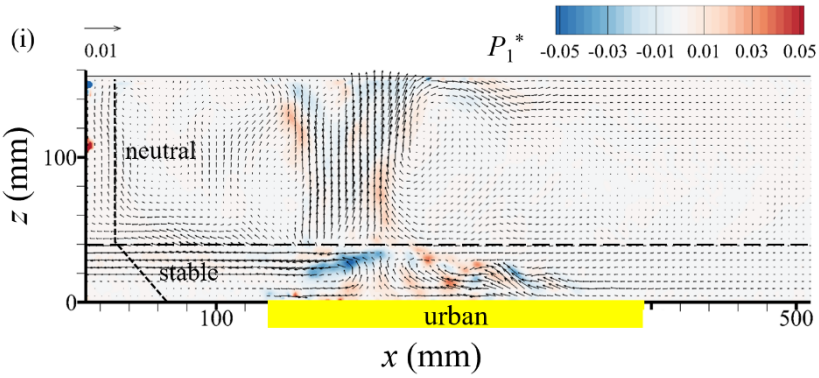
(i)
0.01
P_1^*
-0.05 -0.03 -0.01 0.01 0.03 0.05
neutral
stable
urban
100
0
100
500
z (mm)
x (mm)

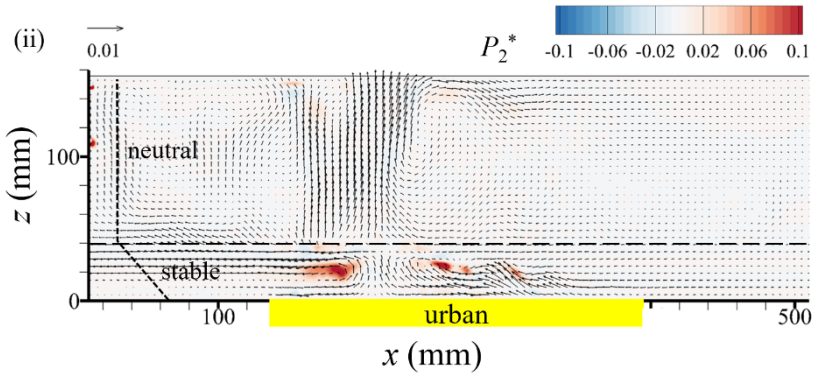
(ii)
0.01
P_2^*
-0.1 -0.06 -0.02 0.02 0.06 0.1
neutral
stable
urban
100
0
100
500
z (mm)
x (mm)

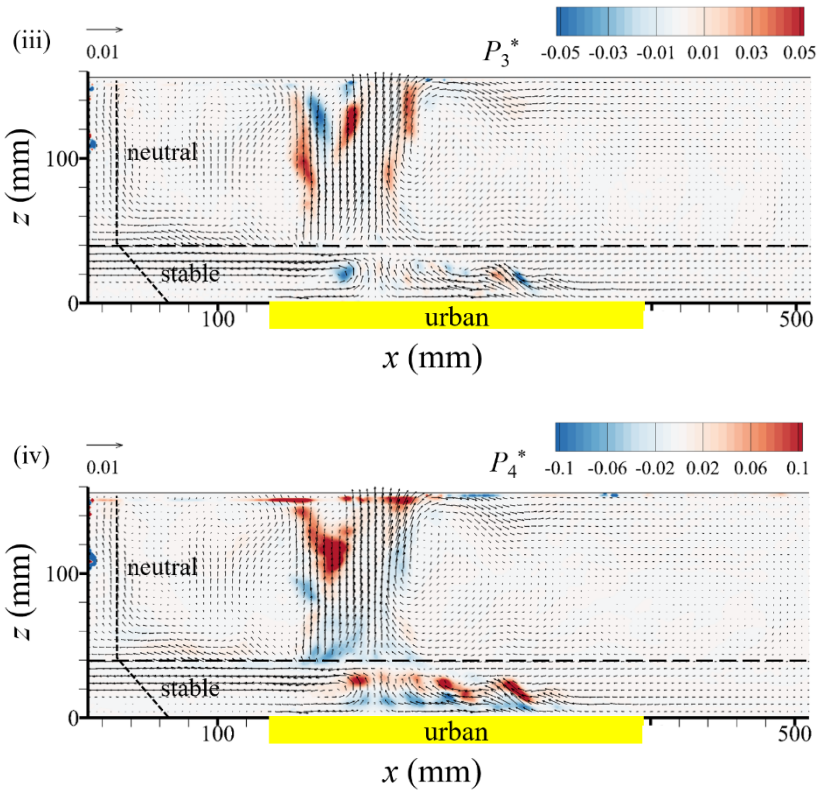

(f)

Figure A1. Non-dimensional turbulence production terms (P_1^* to P_4^*) in (a) Case 1, (b) Case 2, (c) Case 3, (d) Case 4, (e) Case 5 and (f) Case 6.

Figure 1. Illustration of the (a) dispersion and (b) fumigation resulting from inversion breakup. (a)(i) A polluted dome is formed in a stable layer due to ground-based pollution. (a)(ii) Inversion breakup reduces the pollutant concentration. (b)(i) A polluted layer is formed above the urban dome due to the elevated pollutant sources. (b)(ii) Inversion breakup brings the upper-level pollutants to the ground. Not to scale in the vertical direction.

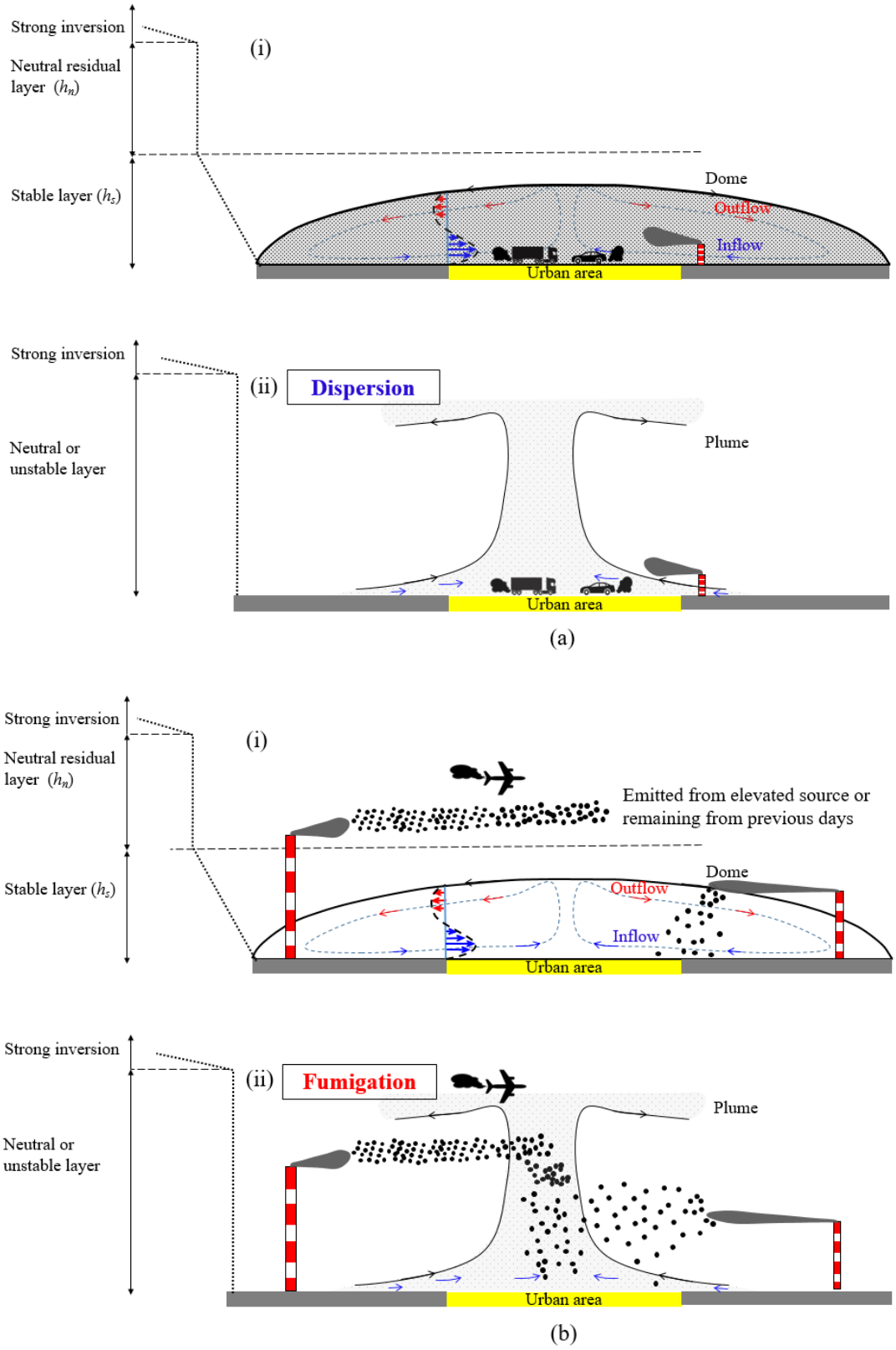

Figure 2. Schematics of the experimental setup. (a) Overall size of the water tank and measuring planes. (b) Cross-section of the water tank heating system for simulating the urban heating process.

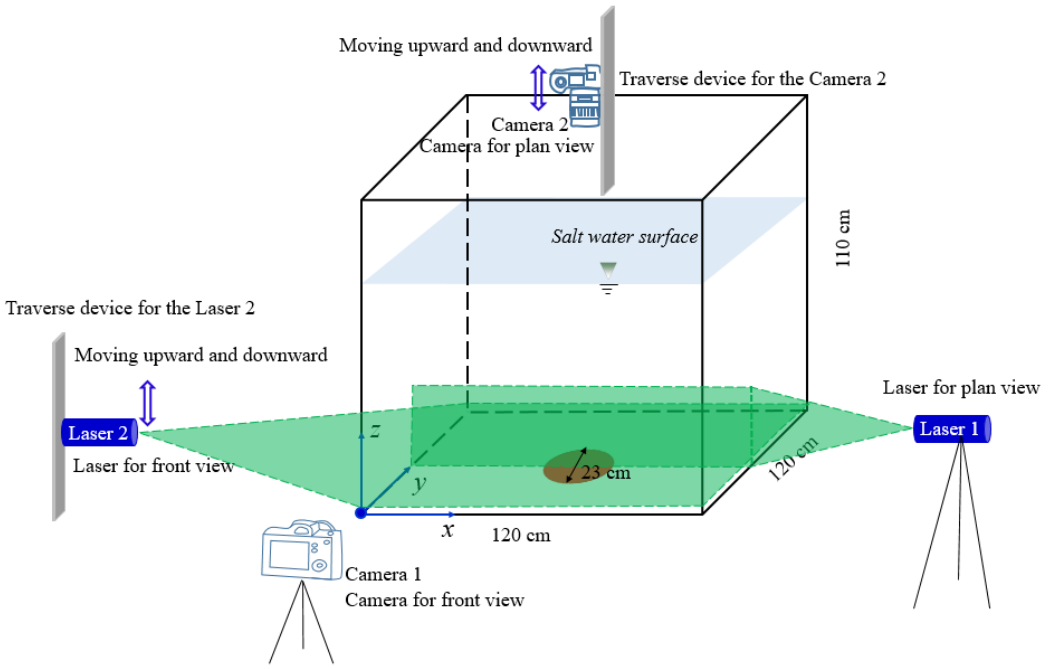

(a)

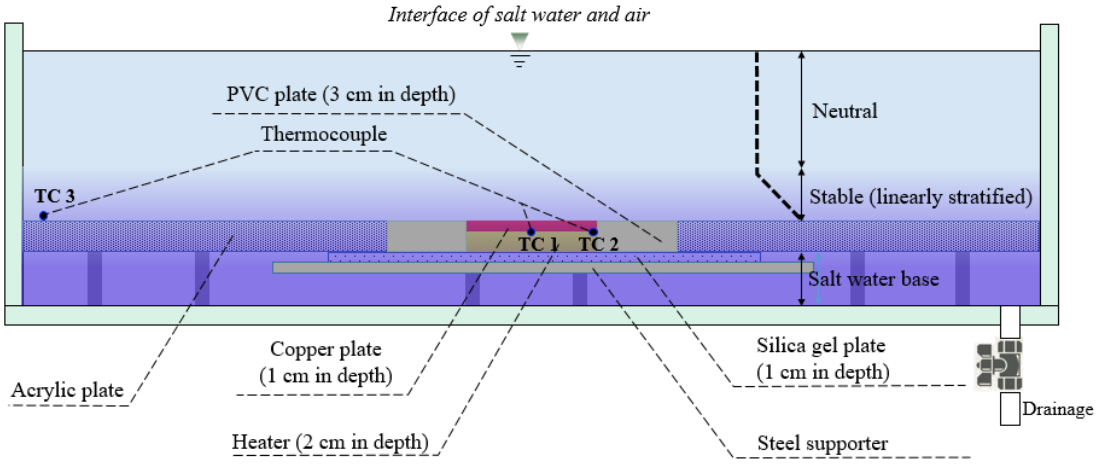

(b)

Figure 3. Shape and layout of urban areas in the six cases.

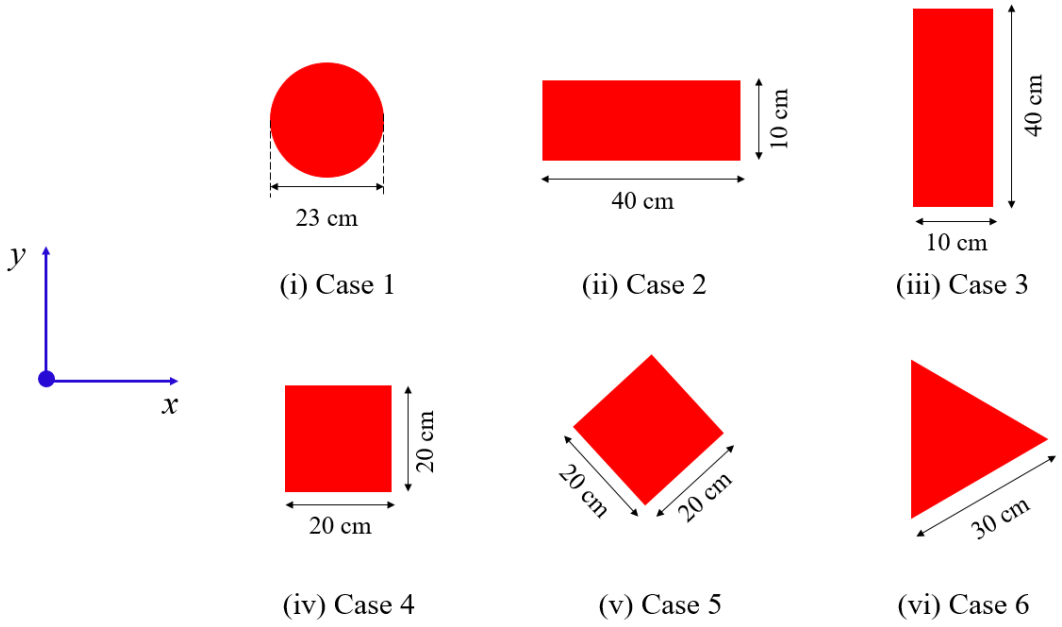

Figure 4. Density profiles of the six cases.

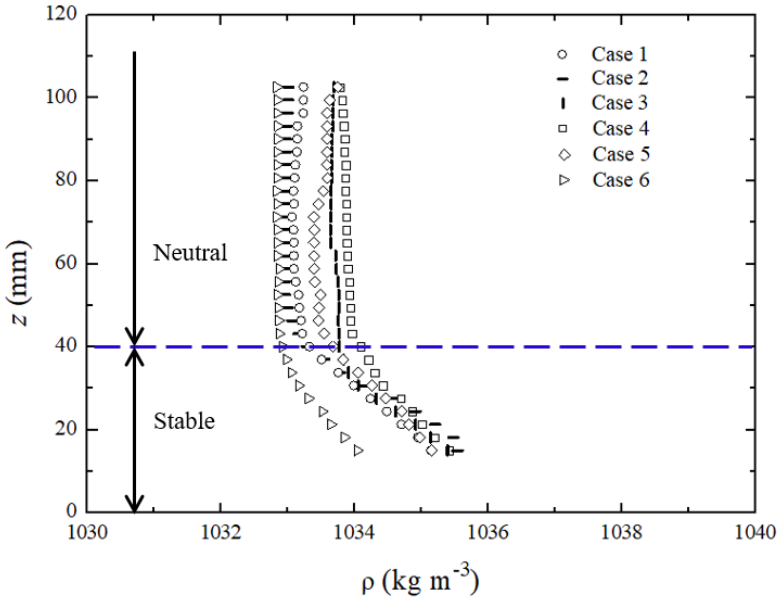

Figure 5. Mean velocity field on a vertical plane across the centre of the urban area in (a) Case 1, (b) Case 2, (c) Case 3, (d) Case 4, (e) Case 5 and (f) Case 6.

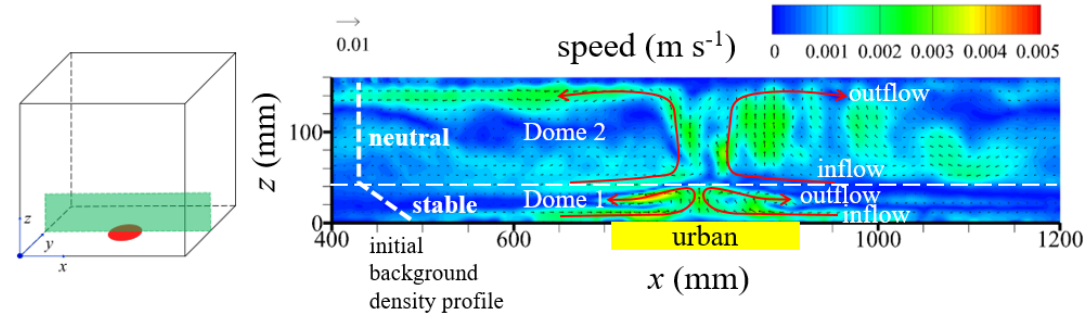
0.01
speed (m s-1)
0 0.001 0.002 0.003 0.004 0.005
z (mm)
100
0
neutral
Dome 2
outflow
inflow
stable
Dome 1
outflow
inflow
400
600
urban
1000
1200
initial
background
density profile
x (mm)

(a)

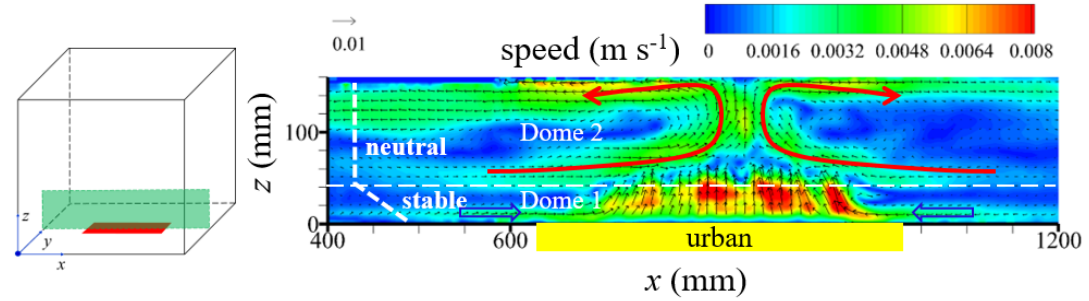
0.01
speed (m s-1)
0 0.0016 0.0032 0.0048 0.0064 0.008
z (mm)
100
0
neutral
Dome 2
stable
Dome 1
400
600
urban
1200
x (mm)

(b)

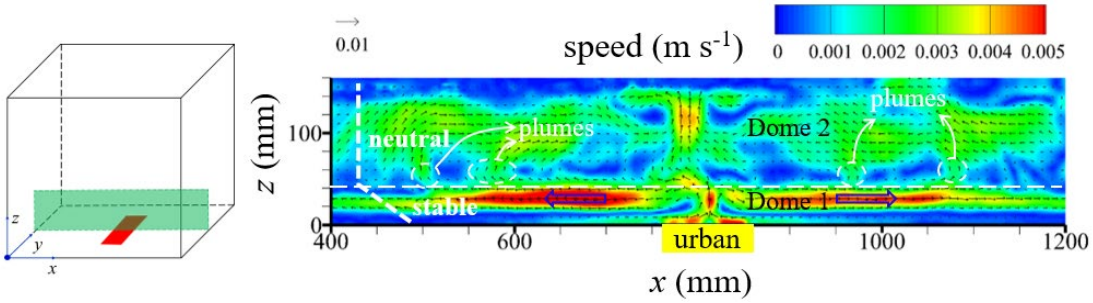
0.01
speed (m s-1)
0 0.001 0.002 0.003 0.004 0.005
z (mm)
100
0
neutral
plumes
Dome 2
plumes
stable
Dome 1
400
600
urban
1000
1200
x (mm)

(c)

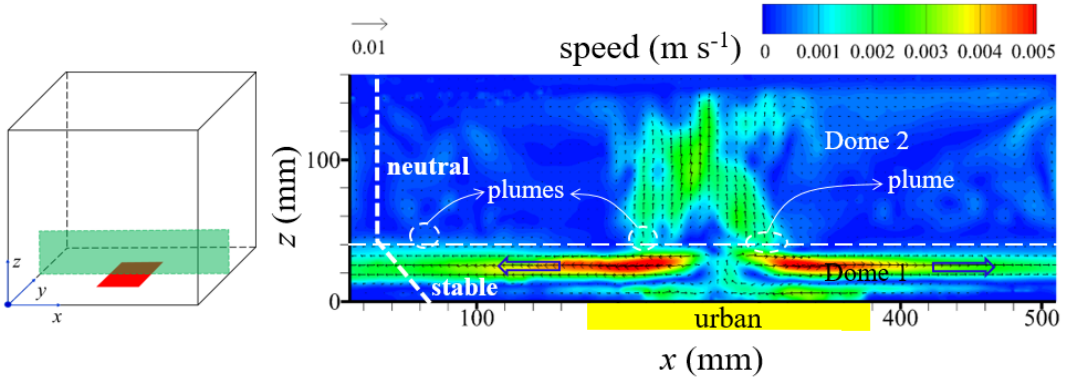
0.01
speed (m s-1)
0 0.001 0.002 0.003 0.004 0.005
z (mm)
100
0
neutral
plumes
Dome 2
plume
stable
Dome 1
100
urban
400
500
x (mm)

(d)

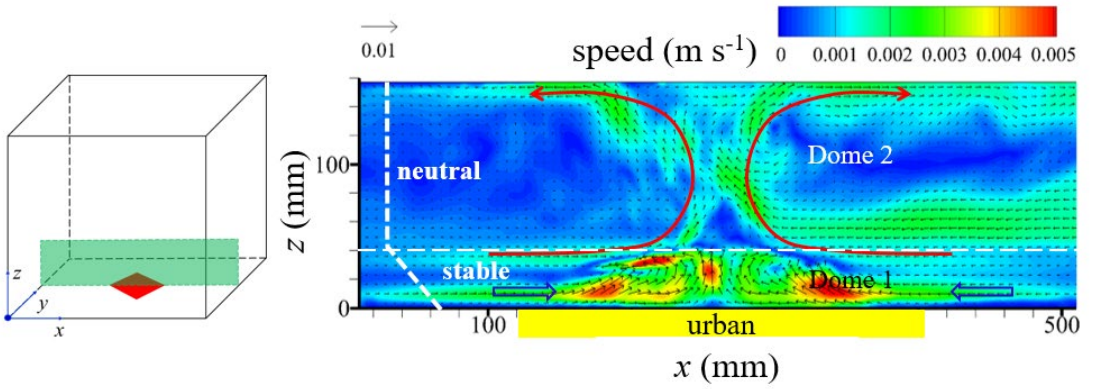

(e)

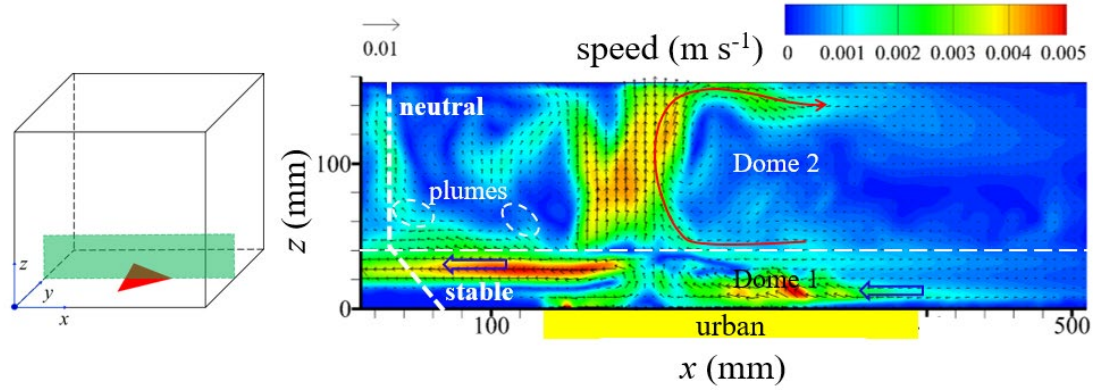

(f)

Figure 6. (a) Schematic of the measured horizontal planes over a rectangular urban area. Velocity fields on horizontal planes (b) 5 mm, (c) 30 mm and (d) 40 mm above the urban surface.

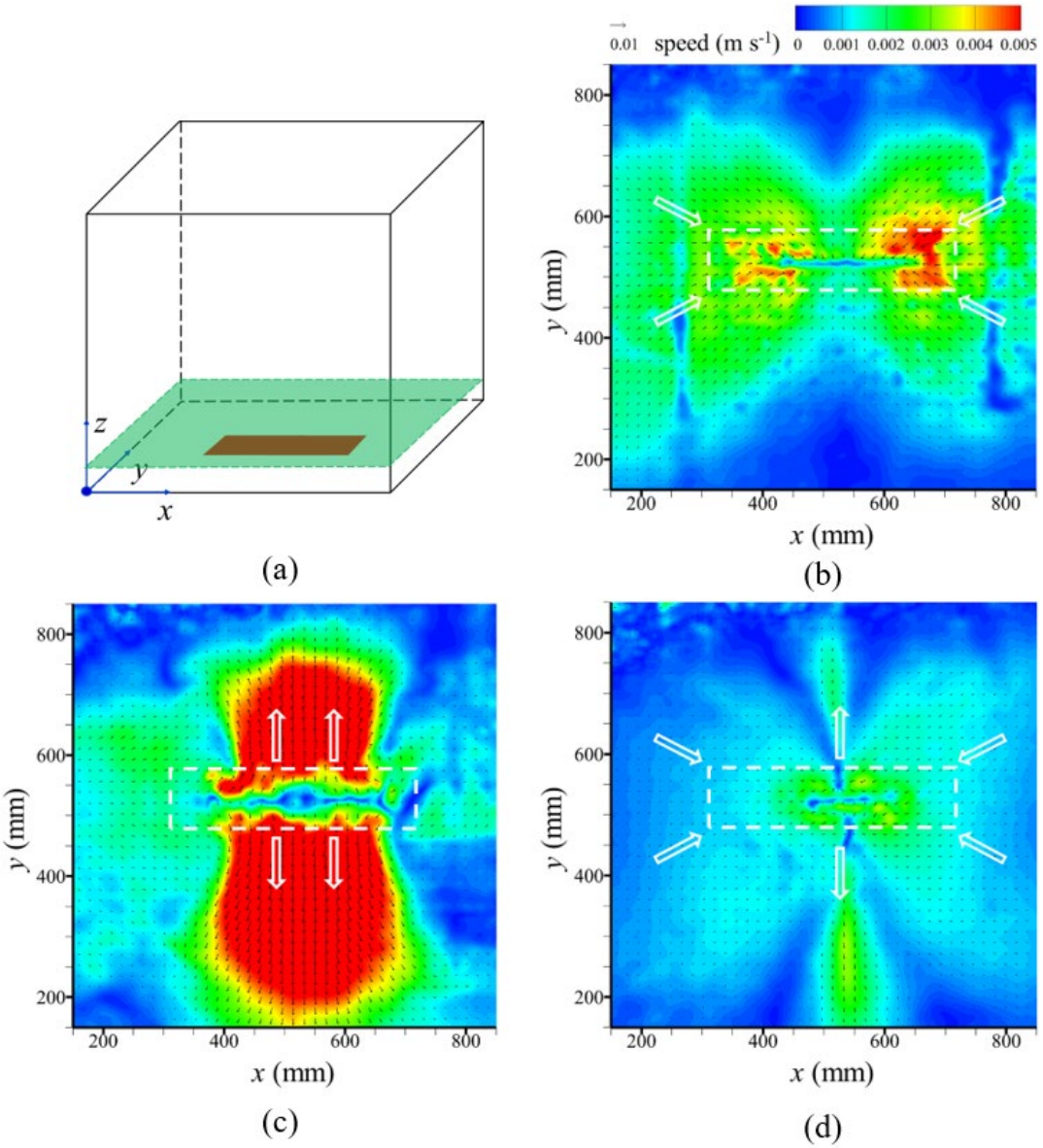

Figure 7. (a) Schematic of the measured horizontal planes over a square urban area. Velocity fields on horizontal planes (b) 10 mm, (c) 25 mm and (d) 40 mm above the urban surface.

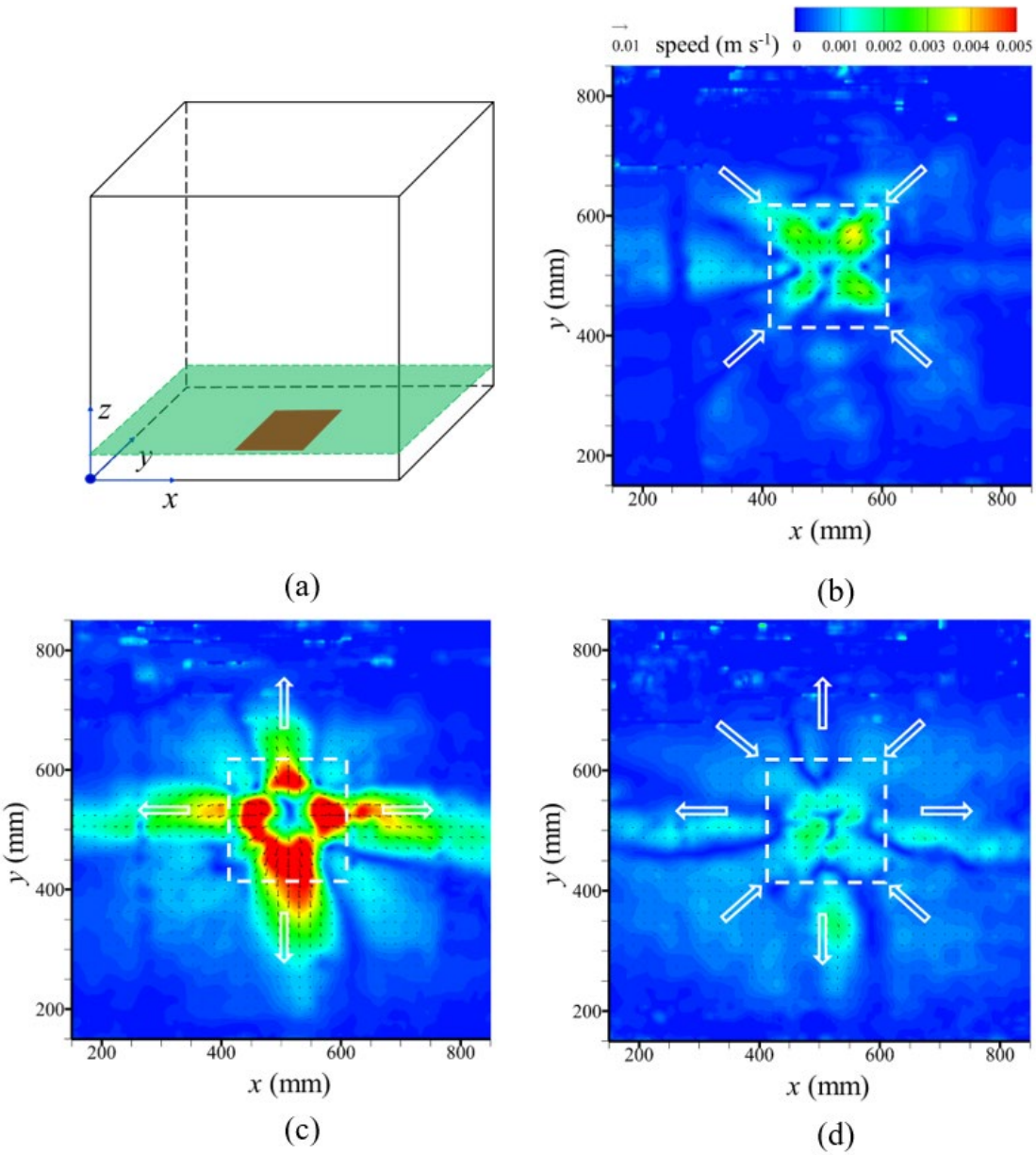

Figure 8. (a) Schematic of the measured horizontal planes over a triangular urban area. Velocity fields on horizontal planes (b) 5 mm, (c) 20 mm and (d) 40 mm above the urban surface.

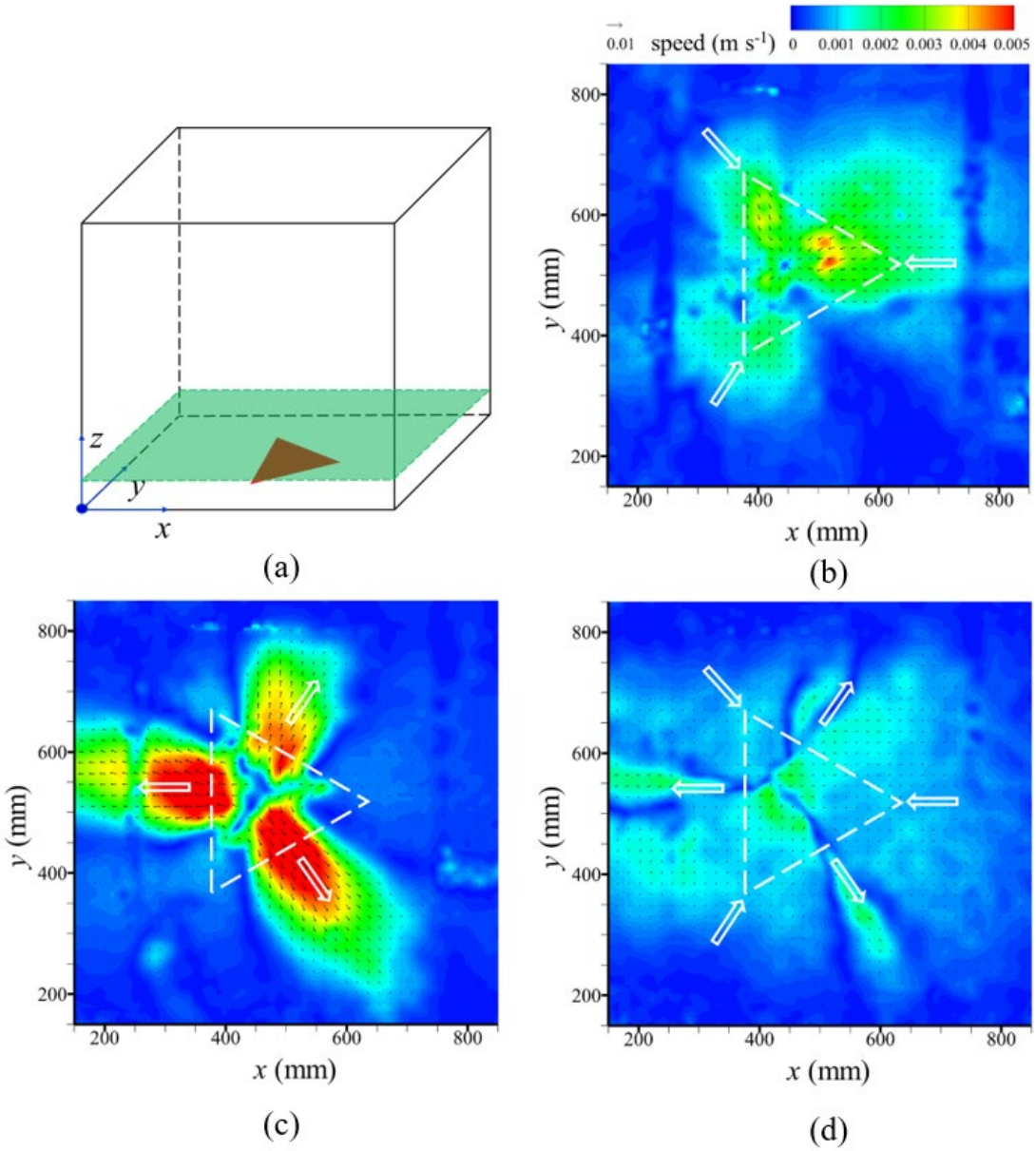

Figure 9. TKEs of (a) Case 1, (b) Case 2, (c) Case 3, (d) Case 4, (e) Case 5 and (f) Case 6.

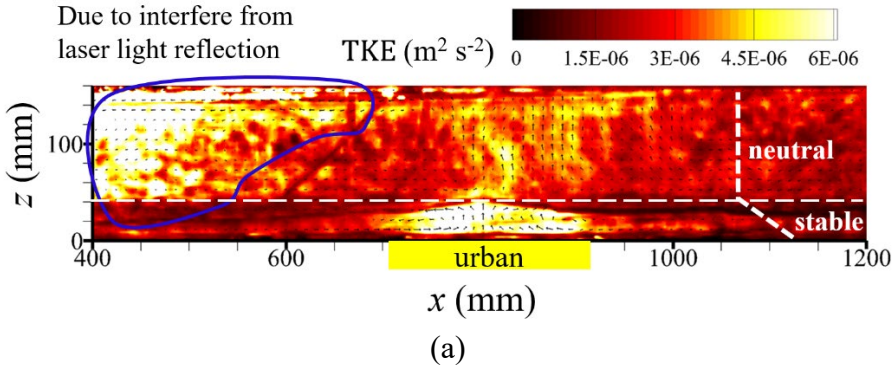

(a)

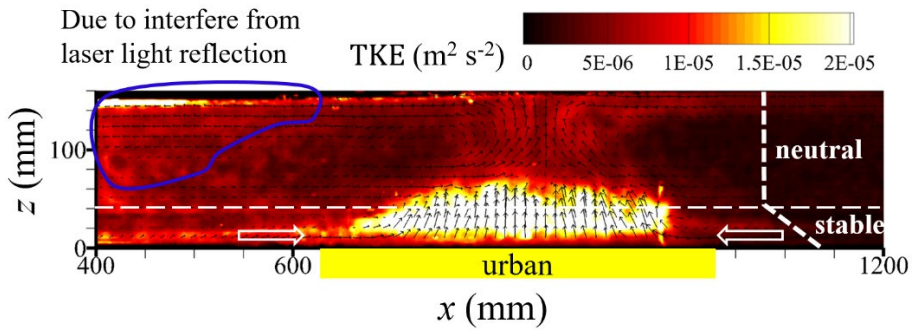
Due to interfere from
laser light reflection
TKE (m² s⁻²)
0
5E-06
1E-05
1.5E-05
2E-05
z (mm)
100
0
neutral
stable
400
600
urban
1200
x (mm)

(b)

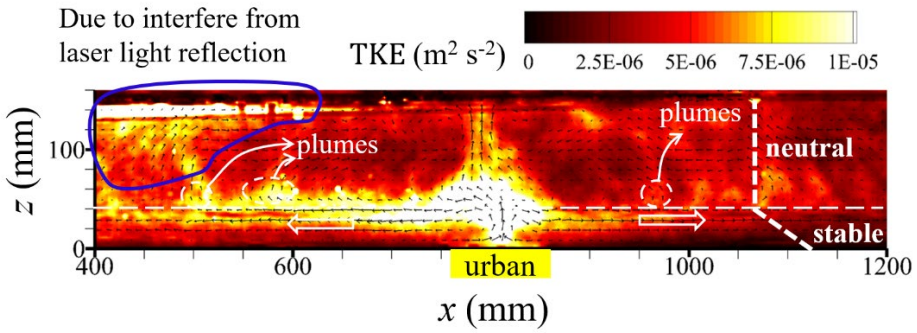
Due to interfere from
laser light reflection
TKE (m² s⁻²)
0
2.5E-06
5E-06
7.5E-06
1E-05
z (mm)
100
0
plumes
plumes
neutral
stable
400
600
urban
1000
1200
x (mm)

(c)

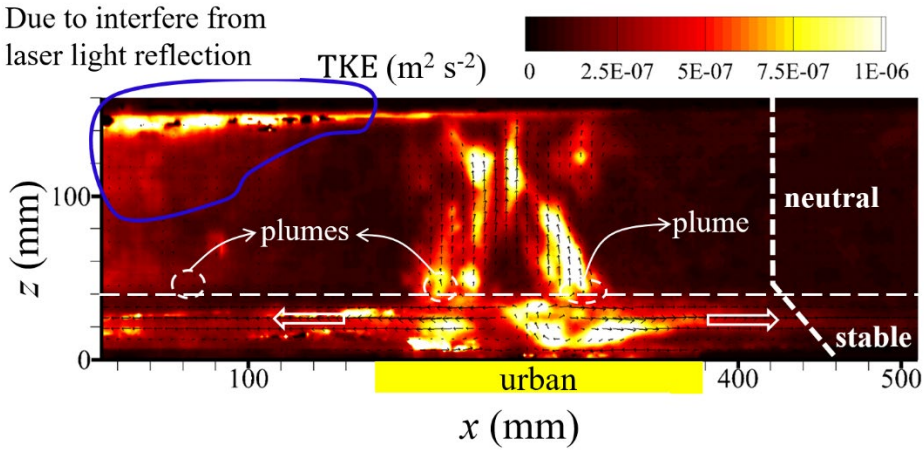
Due to interfere from
laser light reflection
TKE (m² s⁻²)
0
2.5E-07
5E-07
7.5E-07
1E-06
z (mm)
100
0
plumes
plume
neutral
stable
100
urban
400
500
x (mm)

(d)

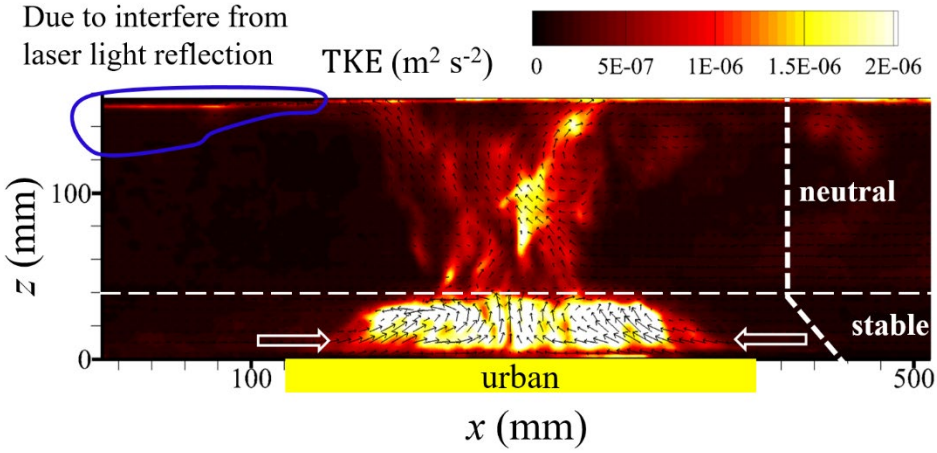
Due to interfere from
laser light reflection
TKE (m² s⁻²)
0
5E-07
1E-06
1.5E-06
2E-06
z (mm)
100
0
neutral
stable
100
urban
500
x (mm)

(e)

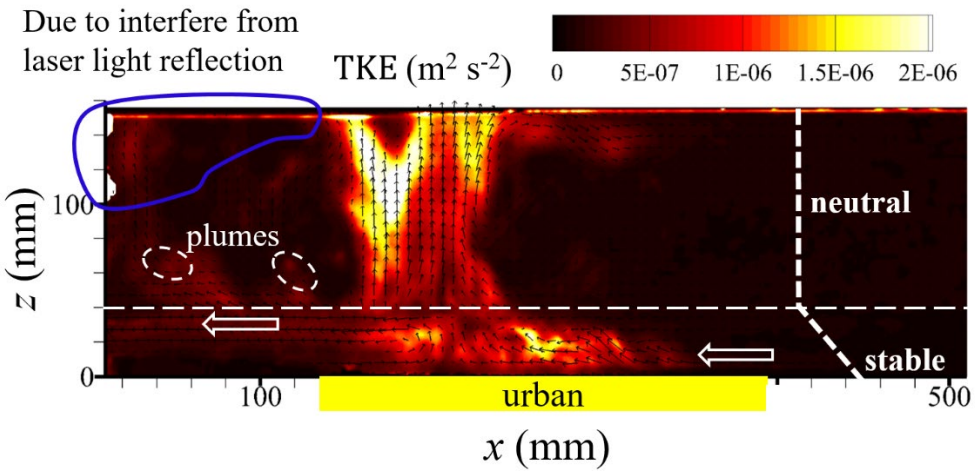

(f)

Figure 10. Momentum flux in (a) Case 1, (b) Case 2, (c) Case 3, (d) Case 4, (e) Case 5 and (f) Case 6.

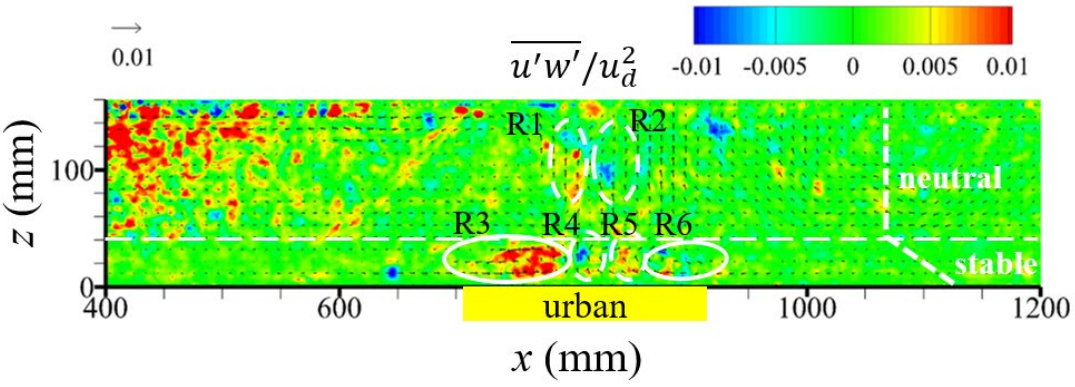

(a)

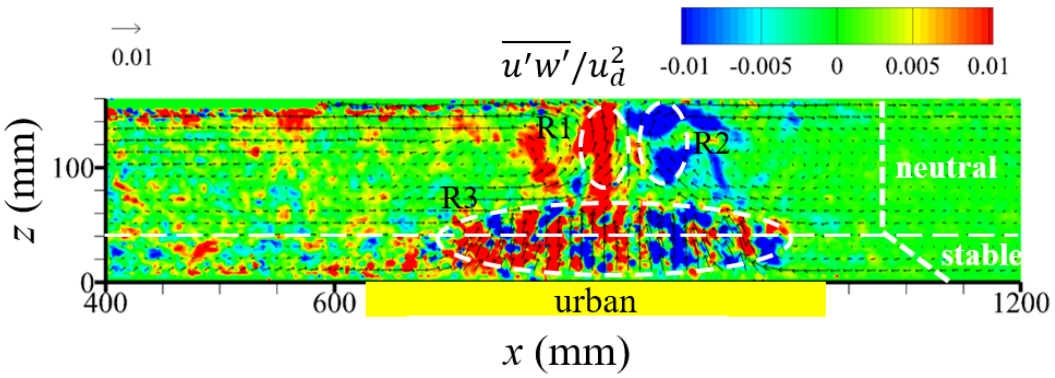

(b)

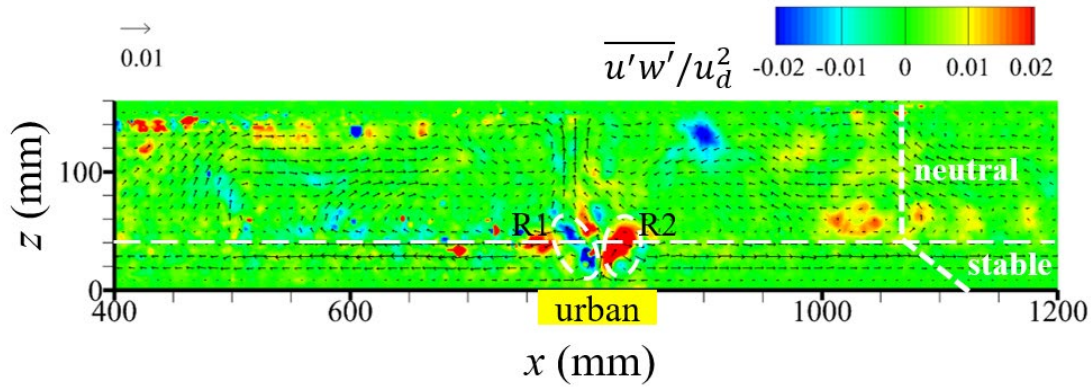
0.01
$\overline{u'w'}/u_d^2$
-0.02 -0.01 0 0.01 0.02
z (mm)
100
0
R1
R2
neutral
stable
400
600
urban
1000
1200
x (mm)

(c)

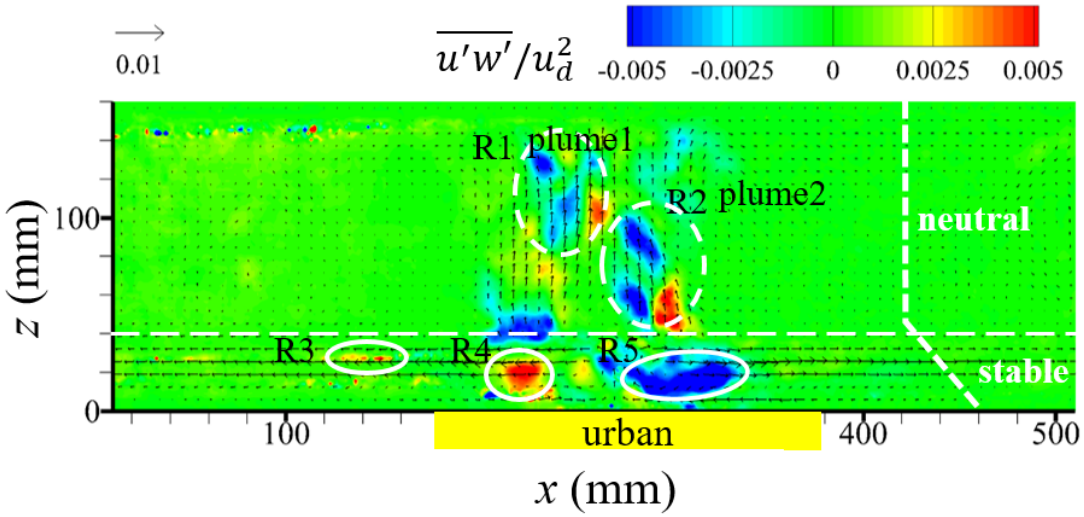
0.01
$\overline{u'w'}/u_d^2$
-0.005 -0.0025 0 0.0025 0.005
R1
plume1
R2
plume2
neutral
z (mm)
100
0
R3
R4
R5
stable
100
urban
400
500
x (mm)

(d)

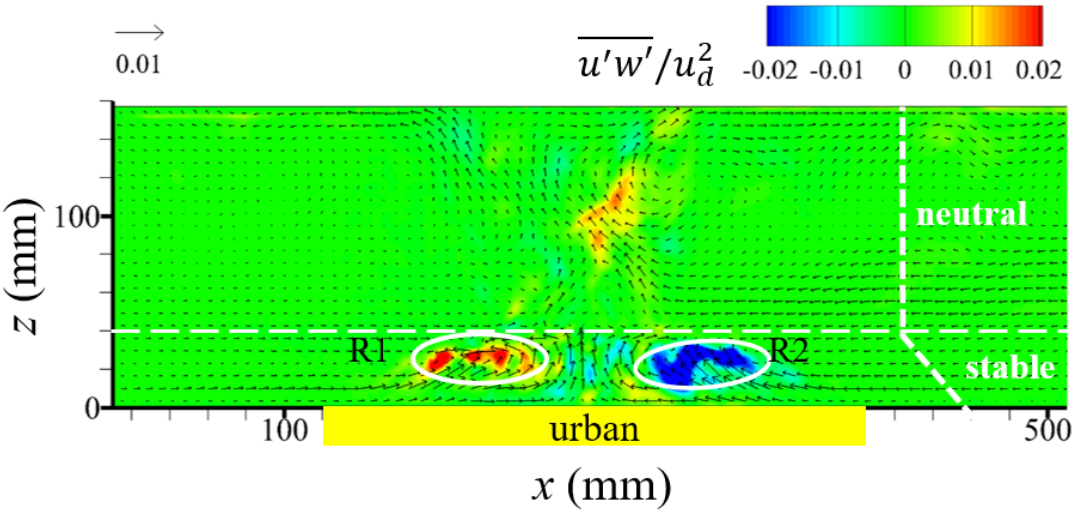
0.01
$\overline{u'w'}/u_d^2$
-0.02 -0.01 0 0.01 0.02
neutral
z (mm)
100
0
R1
R2
stable
100
urban
500
x (mm)

(e)

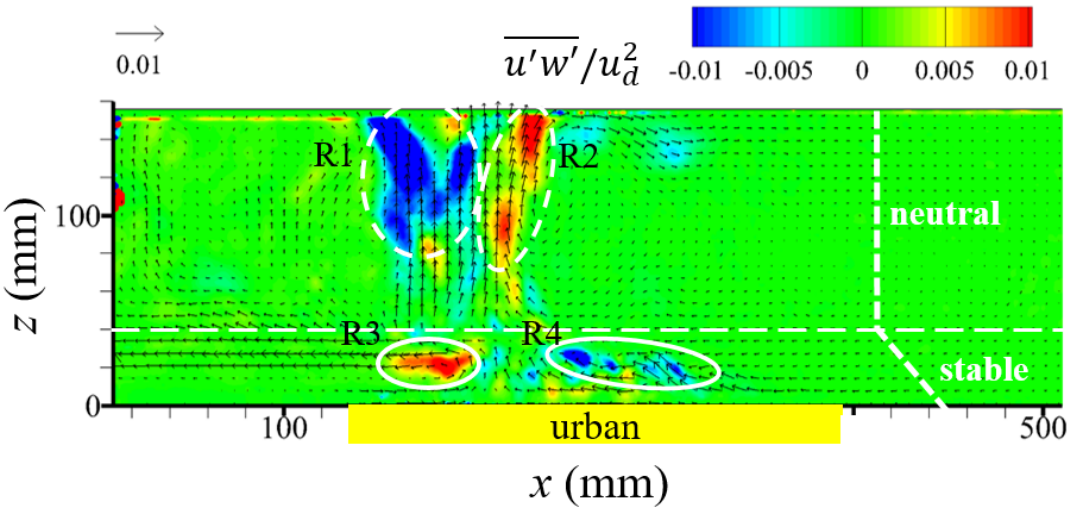

(f)

Figure 11. Non-dimensional turbulence production (P_{all}^*) in (a) Case 1, (b) Case 2, (c) Case 3, (d) Case 4, (e) Case 5 and (f) Case 6.

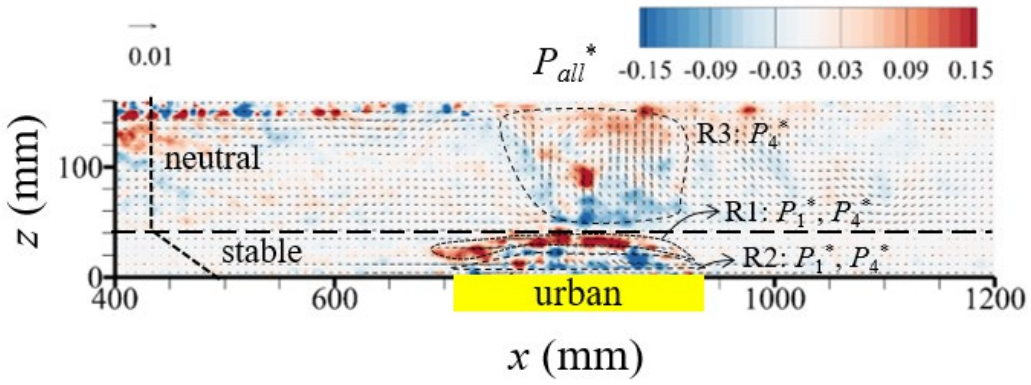

(a)

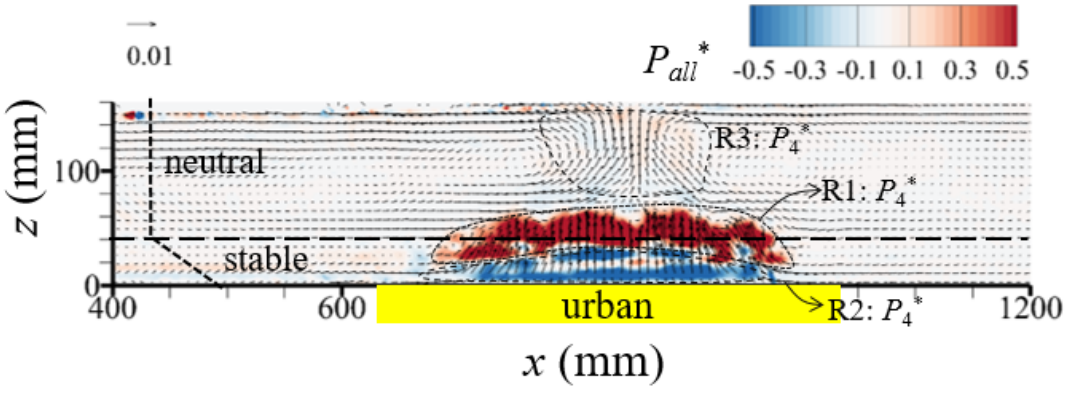

(b)

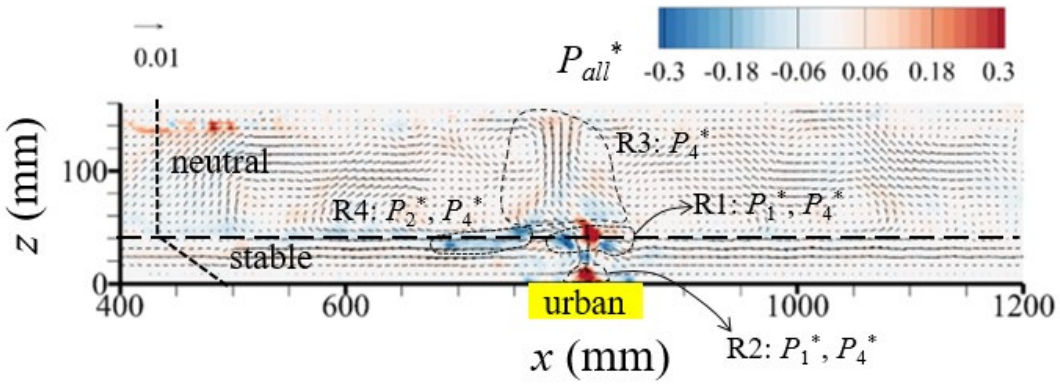
0.01
P_{all}^*
-0.3 -0.18 -0.06 0.06 0.18 0.3
neutral
stable
R3: P_4^*
R4: P_2^*, P_4^*
R1: P_1^*, P_4^*
R2: P_1^*, P_4^*
urban
z (mm)
x (mm)
0
100
400
600
1000
1200

(c)

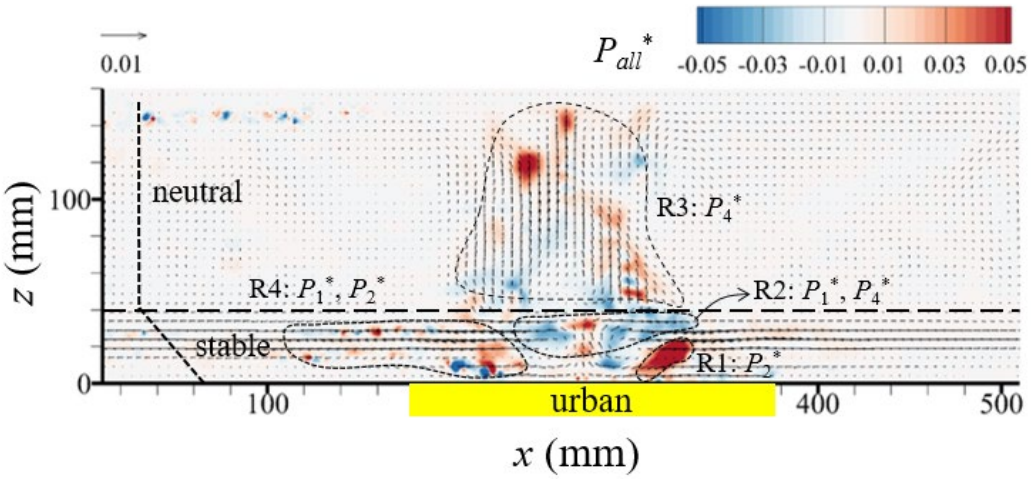
0.01
P_{all}^*
-0.05 -0.03 -0.01 0.01 0.03 0.05
neutral
stable
R3: P_4^*
R4: P_1^*, P_2^*
R2: P_1^*, P_4^*
R1: P_2^*
urban
z (mm)
x (mm)
0
100
400
500

(d)

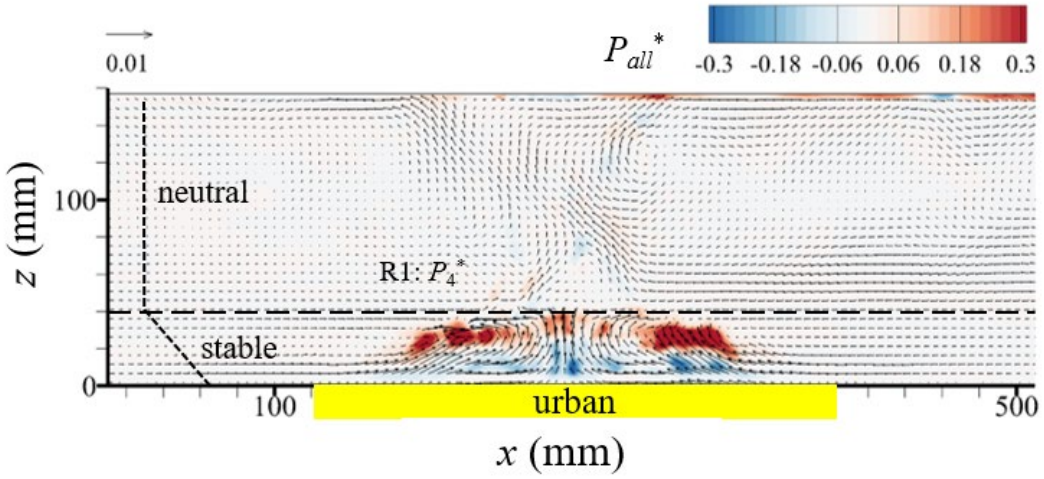
0.01
P_{all}^*
-0.3 -0.18 -0.06 0.06 0.18 0.3
neutral
stable
R1: P_4^*
urban
z (mm)
x (mm)
0
100
500

(e)

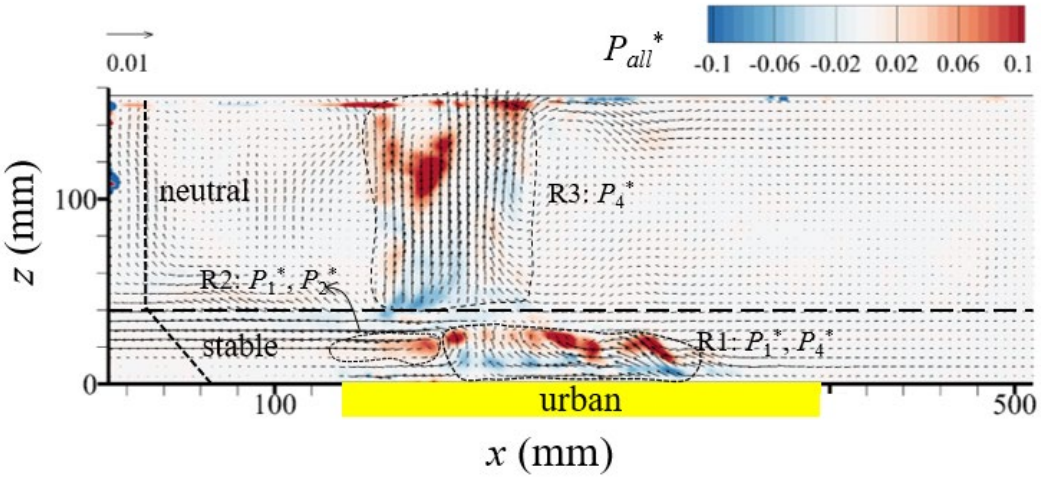
0.01
P_{all}^*
-0.1 -0.06 -0.02 0.02 0.06 0.1
neutral
R3: P_4^*
R2: P_1^*, P_2^*
stable
R1: P_1^*, P_4^*
urban
z (mm)
x (mm)
0
100
100
500

(f)

Table 1. Experimental parameters used in the six cases.

Case No.	d (m)	N (s^{-1})	P_s (W m^{-2})	T_s (℃)	T_a (℃)	P_l (W m^{-2})	H_0 (W m^{-2})	u_d (m s^{-1})	Fr
1	0.23	0.84	5523	34.9	22.7	207	5316	0.0091	0.047
2	0.16	0.94	15000	59.8	24.1	607	14393	0.0112	0.075
3	0.16	0.90	15000	58.9	22.3	622	14378	0.0112	0.078
4	0.20	0.71	5508	37.1	22.0	257	5251	0.0086	0.060
5	0.20	0.75	5508	37.8	23.1	250	5258	0.0086	0.057
6	0.18	0.72	5531	34.5	22.8	198	5333	0.0083	0.065